https://doi.org/10.5194/egusphere-2026-1658
Preprint. Discussion started: 20 April 2026

Hybrid implicit–explicit XFEM simulation of injection-induced seismicity: resolving multi-scale rupture nucleation and dynamics

Mohammad Sabah[1], Mauro Cacace[2], Inga Berre[3], Iman R. Kivi[4], Hannes Hofmann[1,2]

[1] Institute for Applied Geosciences, Technische Universität Berlin, 10587 Berlin, Germany
[2] GFZ Helmholtz Centre for Geosciences, Telegrafenberg, 14473 Potsdam, Germany
[3] Center for Modeling of Coupled Subsurface Dynamics, Department of Mathematics, University of Bergen, 5020 Bergen, Norway
[4] Department of Earth Science and Engineering, Imperial College London, SW7 2AZ London, UK

Correspondence to: Mohammad Sabah (m.sabah@campus.tu-berlin.de)

Abstract. This study introduces a new hybrid implicit–explicit (IMEX) time-integration method for simulating injection-induced fault reactivation within a fully coupled hydromechanical extended finite element (XFEM) framework. Modeling these systems is inherently difficult because of the extreme difference in temporal scales—ranging from days for fluid diffusion to less than milliseconds for dynamic rupture. While fully implicit schemes provide unconditional stability, our results show that numerical accuracy during rupture nucleation is strictly controlled by the minimum time step used. Under-resolving these rapid transients causes delayed instability, lower slip rates, and underestimated seismic moments. Importantly, the temporal resolution needed to accurately capture rupture propagation is approximately the same as the critical time step set by the Courant–Friedrichs–Lewy (CFL) condition. To address this, the proposed IMEX strategy uses an implicit solver for quasi-static loading and switches smoothly to a fully dynamic explicit update once a slip-velocity threshold is reached. This hybrid approach significantly reduces computational costs—by 60–77% compared to fully implicit simulations—while still accurately capturing fault slip, stress changes, and seismic magnitudes. Fully implicit solutions tend to predict slightly higher peak slip velocities and rupture speeds, but event timing and final deformation are consistent across both methods. Additionally, we show that the efficiency of the IMEX framework scales independently of the calculation of the complex slip tangent operator, providing a robust and efficient solution for multi-scale subsurface hazard assessment.

1 Introduction

The increasing reliance on subsurface technologies such as enhanced geothermal systems (EGS), carbon capture and storage (CCS), and deep wastewater disposal has become a cornerstone of modern energy transition and climate-mitigation strategies. Despite their societal benefits, these operations inevitably involve large-scale fluid injection into the crust, which has been repeatedly associated with injection-induced seismicity (Cao et al., 2022; Grigoratos et al., 2022; Cheng et al., 2023; Templeton et al., 2023; Zhou et al., 2024; Sun et al., 2026). Induced seismicity poses significant operational, regulatory, and societal challenges (Grigoli et al., 2017; Trutnevyte & Ejderyan, 2018; Bommer, 2022), particularly when events exceed acceptable risk thresholds. Consequently, accurately simulating the mechanisms controlling the timing, magnitude, and spatial evolution of induced earthquakes remains a key scientific and engineering objective.

Injection-induced seismicity arises from the coupled interactions of multiple physical processes, including pore-pressure diffusion, thermoporoelastic stress redistribution, and frictional weakening along pre-existing faults (Boyet et al., 2023; Kivi et al., 2023). Capturing this complexity in numerical models requires to fully resolve the details of the coupling among these physical processes while also incorporating advanced fracture constitutive laws that govern fault strength and deformation (Cueto-Felgueroso et al., 2018; Riga & Turuntaev, 2021; Heimisson et al., 2022; Ito et al., 2023; Gerardi et al., 2024; Ito et al., 2024; Im & Avouac, 2025; Hosseini et al., 2025). While significant progress has been made in describing frictional fault behavior, its practical application to realistic injection scenarios remains computationally demanding.

https://doi.org/10.5194/egusphere-2026-1658
Preprint. Discussion started: 20 April 2026

A key challenge stems from the extreme separation of temporal scales inherent to injection-driven fault reactivation. Reservoir pressurization and fluid diffusion typically evolve over hours to days, whereas fault nucleation and dynamic rupture unfold over less than milliseconds to seconds (Han & Younis, 2023). Accurately resolving both regimes within a single simulation places stringent demands on time-integration schemes. Fully implicit methods are commonly adopted because of their unconditional stability and efficiency during long periods of quasi-static loading (Jin & Zoback, 2018; Romanet et al., 2025). However, once rapid fault acceleration begins, these schemes require very small time steps and repeated global Newton iterations to maintain accuracy, leading to prohibitive computational costs. In contrast, explicit schemes are well suited for dynamic rupture due to their low per-step cost and straightforward treatment of inertia, but their strict Courant–Friedrichs–Lewy (CFL) stability constraint (Alkhimenkov et al., 2021) renders them impractical for simulating long-term fluid injection and slow nucleation phases.

This fundamental trade-off between stability, accuracy, and efficiency reveals a methodological gap: no single time-integration method is optimal for all processes involved in injection-induced seismicity. Overcoming this limitation is essential for creating physics-based simulations that are both accurate during rupture and manageable over operational time scales. To address this, we introduce and implement, for the first time in the context of injection-induced seismicity, a unified hybrid implicit–explicit (IMEX) time-integration framework within a fully coupled hydromechanical XFEM formulation. The approach advances the system implicitly during quasi-static loading and nucleation, then automatically switches to a fully dynamic explicit formulation once a slip-velocity threshold, indicating unstable rupture, is exceeded. This physics-based switching enables a consistent and adaptive treatment of multi-scale processes within a single computational model. The implicit formulation presented here serves as a robust reference solution and represents a significant improvement over previous efforts in modeling fault rupture processes. (Sabah et al., 2026). Building on this foundation, we show that the IMEX strategy preserves the accuracy of fault slip, stress evolution, and seismic source parameters while significantly reducing computational costs under changing subsurface conditions.

The rest of the paper is organized as follows. Section 2 explains the methodological framework, including the coupled hydromechanical equations, rate-and-state friction model, and XFEM-based spatial discretization. This section also introduces the reference fully implicit scheme, a modified version of our previous work, and the hybrid IMEX strategy with its switching criteria. Section 3 discusses the model validation, including benchmark problems used to verify the coupled formulation and numerical implementation, and outlines the numerical model setup, including geometry, material properties, and injection protocols. Section 4 presents numerical experiments that evaluate the impact of time-stepping on the implicit solver and compare the IMEX formulation with the reference regarding accuracy and performance. Finally, Section 5 summarizes our conclusions and discusses future extensions to 3D systems.

2 Mathematical formulation

2.1 Governing equations

The partial differential equations governing the dynamics of isothermal deformation of faults in a porous medium include both the mechanical equilibrium of the solid-fluid system and the mass conservation laws that govern fluid flow through the faults and the surrounding porous matrix. The equation describing the balance of linear momentum in a dynamic context is formulated within the framework of poroviscoelasticity, in which the solid matrix is modeled as a Kelvin-Voigt (KV) material. This formulation captures the intrinsic damping of natural rocks and introduces rate dependence that helps regularize the problem and mitigate numerical instabilities associated with strain localization (Hayek et al., 2023). The momentum equation for the solid-fluid system thus includes inertial forces, body forces, and internal dissipation, and can be written as follows (Jaeger et al., 2009):

https://doi.org/10.5194/egusphere-2026-1658
Preprint. Discussion started: 20 April 2026

$$\nabla \cdot [\mathbb{C}: \boldsymbol{\varepsilon}(\mathbf{u}) + \mathbb{D}: \dot{\varepsilon}(\mathbf{u})] - \rho\ddot{\mathbf{u}} + \rho\mathbf{b} = 0 \quad (1)$$

Where $\mathbb{C}$ and $\mathbb{D}$ denote the fourth-order elastic and viscous constitutive tensors, respectively, and $\boldsymbol{\varepsilon}(\mathbf{u})$ and $\dot{\varepsilon}(\mathbf{u})$ represent the strain and strain-rate tensors. Here, $\ddot{\mathbf{u}}$ is the solid acceleration, $\mathbf{b}$ is the body force vector, and ρ is the density of saturated rock.

Fluid flow in the porous matrix is described by Darcy's law, assuming a constant intrinsic permeability of the pore space. By coupling Darcy's law with the mass conservation principle, the governing equation for fluid flow in a poroelastic medium is obtained as follows (Wang, 2000):

$$\nabla \cdot \left[\boldsymbol{k}\left(-\nabla p - \rho_f\ddot{\mathbf{u}} + \rho_f\mathbf{b}\right)\right] + \alpha\nabla \cdot \dot{\mathbf{u}} + S_s\dot{p} = 0 \quad (2)$$

where p denotes the pore pressure, α is the Biot coefficient, $\boldsymbol{k}$ is the hydraulic mobility tensor, ρ_f is fluid density, and $S_s = \left(\phi C_f + \frac{(\alpha-\phi)(1-\alpha)}{K}\right)$ denotes the specific storage coefficient with and K as porosity and solid bulk modulus, respectively, and C_f as fluid compressibility. Fluid flow within a fault obeys the same governing physical principles as flow in the surrounding porous medium; however, it is described on the lower-dimensional fault interface Γ_d, whose characteristic thickness is several orders of magnitude smaller than that of the bulk domain Ω (Fig. 1). In contrast to the porous matrix, fault permeability is not assumed constant but evolves dynamically in response to variations in its hydraulic aperture. This behavior is described by the cubic law, which relates laminar flow along the fault to the cube of the fault's aperture. Accordingly, fluid flow along the fault interface is governed by (Zimmerman & Paluszny, 2024):

$$\nabla \cdot \left[\frac{w^2}{12\mu_f}\left(-\nabla p - \rho_f\ddot{\mathbf{u}} + \rho_f\mathbf{b}\right)\right] + \alpha\nabla \cdot \dot{\mathbf{u}} + C_f\dot{p} = 0, \quad \forall \mathbf{u}, p \in \Gamma_d \quad (3)$$

where w represents the hydraulic aperture of the fault and μ_f is fluid viscosity.

2.2 Variational formulation of flow and deformation in a fractured porous medium

The variational (weak) formulation is obtained by multiplying the governing equations by appropriate test functions and integrating over the computational domain. By applying the Gauss–Green theorem in the presence of discontinuities, ensuring traction continuity across the contact interface, and incorporating Biot's theory to consider poromechanical effects at the interface, the weak form of the mechanical equilibrium (Eq. 1) encompasses contributions from both the bulk domain and the interface as:

$$\int_\Omega \nabla\delta\mathbf{u}: \boldsymbol{\sigma} d\Omega + \int_\Omega \delta\mathbf{u} \cdot \rho\ddot{\mathbf{u}} d\Omega + \int_{\Gamma_d} [\delta\mathbf{u}]\mathbf{t} d\Gamma - \int_{\Gamma_d} [\delta\mathbf{u}](p \cdot \mathbf{n}_{\Gamma_d}) d\Gamma - \int_\Omega \delta\mathbf{u} \cdot \rho\mathbf{b} d\Omega$$
$$- \int_{\Gamma_t} \delta\mathbf{u} \cdot \bar{\mathbf{t}} d\Gamma = 0 \quad (4)$$

where $\delta\mathbf{u}$ is the test function for displacement, $\mathbf{n}_{\Gamma_d}$ is the interface unit normal vector, and $\bar{\mathbf{t}}$ is the traction vector on the domain boundaries Γ_t. In an analogous manner, the weak formulation of the fluid flow equation in the porous matrix is derived by multiplying the governing equation (Eq. 2) by the pressure test function δp and integrating over the domain:

$$\int_\Omega \nabla\delta p\boldsymbol{k}\nabla p d\Omega + \int_\Omega \nabla\delta p\boldsymbol{k} \cdot \rho_f\ddot{\mathbf{u}} d\Omega - \int_{\Gamma_d} \delta p\bar{q}_f d\Gamma + \int_\Omega \delta p\alpha\nabla \cdot \dot{\mathbf{u}} d\Omega + \int_\Omega \delta pS_s\dot{p} d\Omega$$
$$- \int_\Omega \nabla\delta p\boldsymbol{k} \cdot \rho_f\mathbf{b} d\Omega + \int_{\Gamma_w} \delta p(\boldsymbol{q} \cdot \mathbf{n}_\Gamma) d\Gamma = 0 \quad (5)$$

https://doi.org/10.5194/egusphere-2026-1658
Preprint. Discussion started: 20 April 2026

where $\bar{q}_f$ represents the fluid flux component normal to the fault interface, describing the exchange of fluid between the fault and the rock matrix. The weak form of the flow continuity equation within the fault is derived by multiplying the test function $\delta p(x,t)$ by Eq. (3) and integrating over the discontinuous fault domain Ω' (as illustrated in Fig. 1), resulting in:

$$\int_{\Omega'} \nabla\delta p \frac{w^2}{12\mu_f} \nabla p d\Omega + \int_{\Omega'} \nabla\delta p \frac{w^2}{12\mu_f} \rho_f \ddot{\mathbf{u}} d\Omega - \int_{\Gamma_d} \delta p \bar{q}_f d\Gamma + \int_{\Omega'} \delta p \alpha \nabla \cdot \dot{\mathbf{u}} d\Omega$$
$$+ \int_{\Omega'} \delta p C_f \dot{p} d\Omega - \int_{\Omega'} \nabla\delta p \frac{w^2}{12\mu_f} \rho_f \mathbf{b} d\Omega = 0 \quad (6)$$

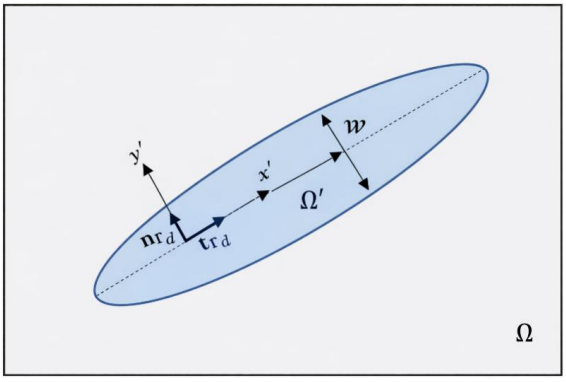

Figure 1: Schematic representation of the local coordinate system and fluid flow geometry within the fault.

Equation (6) provides a unified variational approach for hydro-mechanical coupled fluid flow within faults, allowing for consistent fluid exchange between the fault and the surrounding porous matrix. The formulation is applied over the discontinuous domain cap omega to the prime, using a fault-aligned local coordinate system (Fig. 1). Assuming negligible pressure gradients across the fault aperture, which is justified by the small fault width compared to its length, the cross-sectional integration is simplified by treating pressure as uniform across the aperture (Khoei, 2015):

$$\int_{\Gamma_d} \delta p \bar{q}_f d\Gamma = \int_{\Gamma_d} \nabla\delta p \cdot \mathbf{t}_{\Gamma_d} \left(\frac{w^3}{12\mu_f}\right) \nabla p . \mathbf{t}_{\Gamma_d} d\Gamma + \int_{\Gamma_d} \nabla\delta p \cdot \mathbf{t}_{\Gamma_d} \left(\frac{w^3}{12\mu_f} \rho_f\right) \langle \ddot{\mathbf{u}} \rangle . \mathbf{t}_{\Gamma_d} d\Gamma$$
$$+ \int_{\Gamma_d} \delta p w \, \mathbf{t}_{\Gamma_d} \cdot \langle \nabla \dot{\mathbf{u}} \rangle \cdot \mathbf{t}_{\Gamma_d} d\Gamma + \int_{\Gamma_d} \delta p \, [\dot{\mathbf{u}}] \cdot \mathbf{n}_{\Gamma_d} d\Gamma \quad (7)$$
$$+ \int_{\Gamma_d} \delta p w C_f \dot{p} d\Gamma - \int_{\Gamma_d} \nabla\delta p \cdot \mathbf{t}_{\Gamma_d} \left(\frac{w^3}{12\mu_f} \rho_f\right) \mathbf{b} \cdot \mathbf{t}_{\Gamma_d} d\Gamma$$

where $\mathbf{t}_{\Gamma_d}$ denotes the unit tangent vector along the interface.

2.3 Variational treatment for enforcing contact constraints

The relative normal and tangential displacement between the opposing fault faces, i.e., ${\Gamma_d}^+$ and ${\Gamma_d}^-$, can be defined as follows:

$$g_N = [\![\mathbf{u}]\!] \cdot \mathbf{n}_{\Gamma_d} \quad (8)$$

$$g_T = [\![\mathbf{u}]\!] \cdot \mathbf{t}_{\Gamma_d} \quad (9)$$

where $[\![\mathbf{u}]\!]$ represents the displacement jump across the discontinuity**.** To enforce the unilateral contact condition, the penalty method is commonly employed (Maddio et al., 2025). In this approach, the impenetrability constraint is approximately satisfied by introducing stiff virtual springs at the contact interface. The normal contact force (P_N) is computed as the product of the normal penalty parameter (k_N) and the relative normal displacement (g_N). Likewise, the elastic (stick) component of the

https://doi.org/10.5194/egusphere-2026-1658
Preprint. Discussion started: 20 April 2026

tangential contact force (P_T) is obtained by multiplying the tangential penalty parameter (k_T) with the elastic part of the relative tangential displacement (g_T). The total traction vector on the contact interface can be given by:

$$\mathbf{t} = \left(k_N[\![\mathbf{u}]\!] \cdot \mathbf{n}_{\Gamma_d}\right)\mathbf{n}_{\Gamma_d} + \left(k_T[\![\mathbf{u}]\!] \cdot \mathbf{n}_{\Gamma_d}\right)\mathbf{t}_{\Gamma_d} \tag{10}$$

Assuming the active contact surface $\widetilde{\Gamma_d} \subset \Gamma_d$ is known, the contact pressure and its variation satisfy $\{P_N, \delta P_N\} < 0$ on $\widetilde{\Gamma_d}$ and vanish on the inactive portion $\widetilde{\Gamma_d} \setminus \Gamma_d$. The weak form contribution from the interface integral in Eq. (4) then simplifies to (F. Liu & Borja, 2010):

$$\int_{\Gamma_d} [\delta\mathbf{u}]\mathbf{t}d\Gamma = \int_{\widetilde{\Gamma_d}} [\delta\mathbf{u}]\left(k_N[\![\mathbf{u}]\!] \cdot \mathbf{n}_{\Gamma_d}\right)\mathbf{n}_{\Gamma_d}d\Gamma + \int_{\widetilde{\Gamma_d}} [\delta\mathbf{u}]\left(k_T[\![\mathbf{u}]\!] \cdot \mathbf{n}_{\Gamma_d}\right)\mathbf{t}_{\Gamma_d}d\Gamma \tag{11}$$

To simulate tangential fault deformation during the slip phase, whether seismic or aseismic, a distinct variational formulation is adopted. One of the most widely used criteria for slip, commonly adopted to model frictional contact behavior, is Coulomb's friction law, which is expressed in terms of the contact forces as:

$$r = P_T + \text{sgn}(P_T) f P_N \begin{cases} = 0 & \text{slip condition} \\ < 0 & \text{stick condition} \end{cases} \tag{12}$$

where f is the friction coefficient, which evolves as a function of slip rate and state variables consistent with rate-and-state friction theory. Once slip is detected, the tangential traction magnitude is no longer governed by an elastic resistance but by the interface frictional strength. To efficiently capture the stick-slip transition, a predictor–corrector scheme based on classical plasticity theory is adopted and implemented via a return-mapping algorithm (Fig. 2). During the slip phase, the tangential traction is governed by a rate-dependent constitutive law (F. Liu & Borja, 2009):

$$\dot{P_T} = k_T([\![\dot{\boldsymbol{u}}]\!] \cdot \mathbf{t}_{\Gamma_d} - \dot{\zeta}) \tag{13}$$

where $\dot{\zeta}$ represents the rate of irreversible (plastic) slip. The ζ variable thus quantifies the accumulated tangential plastic slip along the interface. Time integration of the above relation leads to the incremental update of the tangential traction:

$$P_T{}^{n+1} = P_T{}^{n} + k_T([\![\mathbf{u}]\!]^{n+1} - [\![\mathbf{u}]\!]^{n}) \cdot \mathbf{t}_{\Gamma_d} - \text{sgn}(P_T) k_T(\zeta^{n+1} - \zeta^{n}) \tag{14}$$

where superscripts n and $n+1$ denote quantities at the previous and current time steps, respectively. Substituting the updated tangential traction into the sliding condition of Coulomb's friction law leads to the nonlinear residual equation:

$$\begin{aligned} r = {} & P_T{}^{n+1} + \text{sgn}(P_T) f^{n+1} P_N{}^{n+1} - \left(P_T{}^{n} + k_T([\![\mathbf{u}]\!]^{n+1} - [\![\mathbf{u}]\!]^{n}) \cdot \mathbf{t}_{\Gamma_d}\right) \\ & + (\text{sgn}(P_T) k_T(\zeta^{n+1} - \zeta^{n})) + \text{sgn}(P_T) f^{n+1} k_N [\![\mathbf{u}]\!] \cdot \boldsymbol{n}_{\Gamma_d} = 0 \end{aligned} \tag{15}$$

To enforce the nonlinear constraint $r(\zeta) = 0$, a Newton–Raphson iteration is employed, where the Jacobian required for the iterative update is obtained by differentiating Eq. (16) with respect to the plastic slip variable ζ:

$$\frac{\partial r}{\partial \zeta} = r'(\zeta) = \text{sgn}(P_T)\left(-k_T + \frac{\partial f^{n+1}}{\partial \zeta} k_N [\![\mathbf{u}]\!] \cdot \boldsymbol{n}_{\Gamma_d}\right) \tag{16}$$

At each iteration, the derivative of the friction coefficient with respect to the plastic slip must be evaluated. The friction coefficient evolves according to a rate-and-state formulation (Dieterich, 1979; Ruina, 1983):

$$f = \mu_0 + a\, ln\left(\frac{V^{n+1}}{V^*}\right) + b\, ln\left(\frac{\theta^{n+1}}{\theta^*}\right) \tag{17}$$

https://doi.org/10.5194/egusphere-2026-1658
Preprint. Discussion started: 20 April 2026

where V^* denotes the reference slip velocity, while μ^* represents the steady-state friction coefficient. The state variable, θ, characterizes the dependence of friction on both slip time and slip history, whereas θ^* corresponds to its steady-state value when the fault interface is sliding at the reference velocity V^*. The direct effect and friction evolution are denoted by the parameters a and b, respectively. In this work, the evolution of the state variable is governed by the aging law:

$$\dot{\theta} = 1 - \frac{V^{n+1}\theta^{n+1}}{D_c} \tag{18}$$

where D_c is the characteristic slip distance. Applying a backward Euler discretization yields:

$$\theta^{n+1} = \frac{\theta^n + \Delta t}{1 + \frac{\Delta t V^{n+1}}{D_c}} \tag{19}$$

The derivative of the friction coefficient with respect to slip is subsequently obtained using the chain rule:

$$\frac{\partial f}{\partial \zeta} = \frac{\partial f}{\partial V}\frac{\partial V}{\partial \zeta} + \frac{\partial f}{\partial \theta}\frac{\partial \theta}{\partial \zeta} = \frac{1}{\Delta t}\left(\frac{a}{V^{n+1}} - \frac{b}{\theta^{n+1}}\frac{D_c \Delta t(\theta^{n+1}+\Delta t)}{(D_c+\Delta t V^{n+1})^2}\right) \tag{20}$$

The slip variable ζ^{n+1} is iteratively updated until Eq. (15) is satisfied. At each iteration, the slip velocity, state variable, friction coefficient, and its derivative with respect to slip are updated accordingly. Upon convergence, the tangential traction and all internal variables are finalized, ensuring a consistent and physically sound representation of the interface response under evolving frictional conditions.

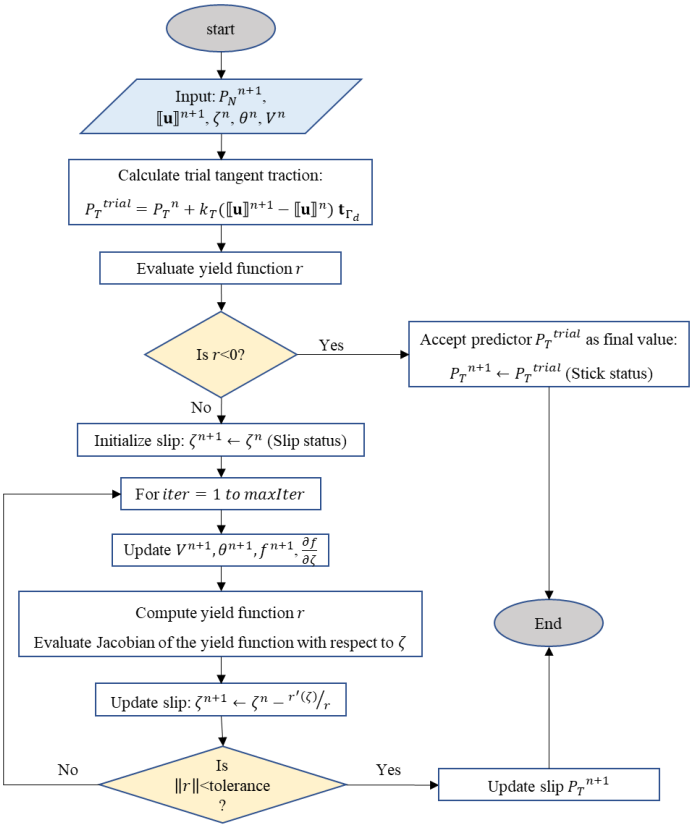

Figure 2: Flowchart of the predictor–corrector return-mapping algorithm used to update tangential traction and slip at the fault interface under rate-and-state friction. The procedure evaluates stick or slip conditions based on a yield criterion, with iterative correction of slip and frictional variables during the slip phase until convergence is achieved.

https://doi.org/10.5194/egusphere-2026-1658
Preprint. Discussion started: 20 April 2026

2.4 Interpolation of pressure and displacement fields

Within the XFEM framework, the displacement field $\mathbf{u}(\boldsymbol{x},t)$ is approximated using an enriched formulation that augments the standard finite element interpolation with additional functions to represent displacement discontinuities and near-tip singularities (Dolbow et al., 2000). The resulting approximation is written as

$$\mathbf{u}^e(\boldsymbol{x},t) = \sum_{i=1}^{\mathcal{N}} N_{uI}(\boldsymbol{x})\overline{\mathbf{u}}_i(t) + \sum_{i=1}^{\mathcal{N}^{Hev}} N_{ui}(\boldsymbol{x})\left(H(\varphi(\boldsymbol{x})) - H\left(\varphi(\boldsymbol{x}_J)\right)\right)\overline{\mathbf{a}}_i(t)$$
$$+ \sum_{i=1}^{\mathcal{N}^{tip}} N_{ui}(\boldsymbol{x}) \sum_{j=1}^{4} \left(T_j(\boldsymbol{x}) - T_j(\boldsymbol{x}_i)\right)\overline{\mathbf{b}}_{ji}(t) \equiv \mathbf{N}_u^{std}(\boldsymbol{x})\overline{\mathbf{u}}(t) + \mathbf{N}_u^{Hev}(\boldsymbol{x})\overline{\mathbf{a}}(t) + \mathbf{N}_u^{tip}(\boldsymbol{x})\overline{\mathbf{b}}(t) \quad (21)$$

where $\mathcal{N}$ denotes all nodal points within element e, and $\mathcal{N}^{Hev}$ and $\mathcal{N}^{tip}$ represent the number of nodes enriched by the Heaviside function and the crack-tip asymptotic functions, respectively. The vectors $\overline{\mathbf{u}}_i(t)$, $\overline{\mathbf{a}}_i(t)$, and $\overline{\mathbf{b}}_{ji}(t)$ correspond to the standard, Heaviside-enriched, and tip-enriched degrees of freedom. The Heaviside enrichment captures the displacement jump across the crack faces, whereas the asymptotic enrichment improves the approximation of the singular displacement field in the vicinity of the crack tip. The crack-tip enrichment functions are defined as (Moës et al., 1999):

$$T(r,\theta) = \{T_1,T_2,T_3,T_4\} = \left\{\sqrt{r}\sin\frac{\theta}{2}, \sqrt{r}\cos\frac{\theta}{2}, \sqrt{r}\sin\frac{\theta}{2}\sin\theta, \sqrt{r}\cos\frac{\theta}{2}\sin\theta\right\} \quad (22)$$

while the Heaviside function is given by

$$H(\varphi(x)) = \begin{cases} +1 & \varphi(x) > 0 \\ -1 & \varphi(x) < 0 \end{cases} \quad (23)$$

where $\varphi(\boldsymbol{x})$ denotes the signed distance function defining the crack geometry, r is the distance from the crack tip, and θ is the polar angle measured from the crack line. The Heaviside enrichment introduces a unit displacement jump across the discontinuity, allowing independent displacement fields on either side of the crack and enabling an accurate representation of strong discontinuities. The displacement jump across the contact surface can be written as:

$$[\![\mathbf{u}]\!] = [\![\mathbf{N}_u^{std}(\boldsymbol{x})\overline{\mathbf{u}}(t) + \mathbf{N}_u^{Hev}(\boldsymbol{x})\overline{\mathbf{a}}(t) + \mathbf{N}_u^{tip}(\boldsymbol{x})\overline{\mathbf{b}}(t)]\!] =$$
$$[\![\mathbf{N}_u^{std}(\boldsymbol{x})\overline{\mathbf{u}}(t)]\!] + [\![\mathbf{N}_u^{Hev}(\boldsymbol{x})\overline{\mathbf{a}}(t)]\!] + [\![\mathbf{N}_u^{Hev}(\boldsymbol{x})\overline{\mathbf{a}}(t)]\!] \quad (24)$$

The term involving the standard shape functions $\mathbf{N}_u^{std}$ vanishes since these functions are continuous across the interface. Consequently, the displacement jump induced by the Heaviside and tip enrichment reduces to:

$$[\![\mathbf{N}_u^{Hev}(\boldsymbol{x})\overline{\mathbf{a}}(t)]\!] = 2\sum_{i=1}^{\mathcal{N}^{Hev}} N_{ui}(\boldsymbol{x})\overline{\mathbf{a}}_i(t) \quad (25)$$

$$[\![\boldsymbol{N}_u^{Hev}(\boldsymbol{x})\overline{\boldsymbol{a}}(t)]\!] = 2\sum_{i=1}^{\mathcal{N}^{tip}} N_{ui}(\boldsymbol{x})\ \sqrt{r}\,\overline{\boldsymbol{b}}_{1i}(t) \quad (26)$$

Among the four crack-tip asymptotic enrichment functions, only the first function generates a displacement discontinuity across the crack faces (Khoei, 2015). The remaining functions primarily enhance the approximation quality in the vicinity of the crack tip and therefore do not contribute to the jump. Based on the XFEM displacement enrichment, the strain field is decomposed into standard, discontinuous, and crack-tip contributions. Accordingly, the strain at position $\boldsymbol{x}$ and time t can be written as:

$$\boldsymbol{\varepsilon}^e(\boldsymbol{x},t) = \sum_{i=1}^{\mathcal{N}} \nabla N_{ui}(\boldsymbol{x})\overline{\mathbf{u}}_i(t) + \sum_{i=1}^{\mathcal{N}^{Hev}} \left((H(\boldsymbol{x}) - H(\boldsymbol{x}_i))\nabla N_{ui}(\boldsymbol{x})\right)\overline{\mathbf{a}}_i(t)$$
$$+ \sum_{i=1}^{\mathcal{N}^{tip}} \nabla N_{ui}(\boldsymbol{x}) \sum_{j=1}^{4} \left(T_j(\boldsymbol{x}) - T_j(\boldsymbol{x}_i)\right)\overline{\mathbf{b}}_{ji}(t) + \sum_{i=1}^{\mathcal{N}^{tip}} N_{ui}(\boldsymbol{x}) \sum_{j=1}^{4} \nabla T_j \overline{\mathbf{b}}_{ji}(t) \quad (27)$$

https://doi.org/10.5194/egusphere-2026-1658
Preprint. Discussion started: 20 April 2026

The evaluation of the spatial derivatives of the crack-tip enrichment functions requires a transformation from the local crack-tip polar coordinate system to the global Cartesian coordinates (x, y) (Khoei, 2015). This transformation can be expressed as:

$$\nabla T_j = \boldsymbol{R}(\theta)\nabla' T_j = \boldsymbol{R}(\theta)\mathbf{J}_{r\theta}\begin{bmatrix} T_{j,r} \\ T_{j,\theta} \end{bmatrix} \tag{28}$$

where $\boldsymbol{R}$ is rotation matrix with θ denoting the angle between the local crack-tip coordinate system (x', y') and the global coordinate axes (x, y), and $\mathbf{J}_{r\theta}$ is the Jacobian relating polar coordinates (r, θ) to the local Cartesian coordinates.

The enriched approximation of the XFEM for the pressure field $p(\boldsymbol{x}, t)$ can be written as:

$$\begin{aligned} p^e(\boldsymbol{x}, t) &= \sum_{i=1}^{\mathcal{N}} N_{p_i}(\boldsymbol{x})\bar{p}_i(t) + \sum_{i=1}^{\mathcal{N}^{mod}} N_{p_i}(\boldsymbol{x})\big(\psi(\boldsymbol{x}) - \psi(\boldsymbol{x}_i)\big)\bar{d}_i(t) \\ &\equiv \mathbf{N}_p^{std}(\boldsymbol{x})\overline{\mathbf{p}}(t) + \mathbf{N}_p^{mod}(\boldsymbol{x})\overline{\mathbf{d}}(t) \end{aligned} \tag{29}$$

where $\bar{p}_i(t)$ denotes the nodal pressure degrees of freedom associated with the standard interpolation, whereas $\bar{d}_i(t)$ denote the additional enriched pressure degrees of freedom introduced to capture non-smooth pressure variations near the interface. The total number of nodes carrying this enrichment is indicated by $\mathcal{N}^{mod}$. The enrichment is constructed using a modified level-set function, defined following Fries & Belytschko (2010) as:

$$\psi(\boldsymbol{x}) = \sum_{i=1}^{\mathcal{N}^{mod}} N_{p_i}(\boldsymbol{x})|\varphi_i| - \left|\sum_{i=1}^{\mathcal{N}^{mod}} N_{pi}(\boldsymbol{x})\varphi_i\right| \tag{30}$$

where ϕ_i are the nodal values of the signed distance function used to describe the interface geometry. This formulation produces an enrichment function that forms a ridge aligned with the interface. As a result, the pressure field remains continuous across the interface, while its spatial gradient is allowed to exhibit a jump. An additional advantage of this construction is that the enrichment naturally vanishes in elements that are not intersected by the interface, thereby eliminating the need for special blending treatments. The pressure gradient inside an enriched element can therefore be evaluated as:

$$\begin{aligned} &\nabla p^e(\boldsymbol{x}, t) = \sum_{i=1}^{\mathcal{N}} \nabla N_{p_i}(\boldsymbol{x})\bar{p}_i(t) + \sum_{i=1}^{\mathcal{N}^{mod}} \nabla N_{p_i}(\boldsymbol{x})\big(\psi(\boldsymbol{x}) - \psi(\boldsymbol{x}_i)\big) + \sum_{i=1}^{\mathcal{N}^{mod}} \nabla N_{p_i}|\varphi_i| \\ &-\mathrm{sgn}\left(\sum_{i=1}^{\mathcal{N}^{mod}} N_{pi}(\boldsymbol{x})\varphi_i\right)\sum_{i=1}^{\mathcal{N}^{mod}} N_{pi}(\boldsymbol{x})\varphi_i N_{pi} \end{aligned} \tag{31}$$

2.5 The XFEM spatial and temporal discretization

By introducing the enriched trial functions for the displacement field (Eq. 21) and the pressure field (Eq. 29), together with their corresponding test functions, and substituting them into the weak formulations given in Eqs. (4) and (5), as well as the relevant interface integral relations, the governing equations can be rearranged into a global matrix form, leading to the following semi-discrete system governing the displacement field:

$$\boldsymbol{M}_{l\times l}\ddot{\boldsymbol{U}}_{l\times 1} + \boldsymbol{D}_{l\times l}\dot{\boldsymbol{u}}_{l\times 1} + \boldsymbol{K}_{l\times l}\boldsymbol{U}_{l\times 1} - \boldsymbol{Q}_{l\times p}\boldsymbol{P}_{p\times 1} + \boldsymbol{F}_{\boldsymbol{int}} - \boldsymbol{F}_{\boldsymbol{ext}} = \mathbf{0} \tag{32}$$

where l denotes the total number of degrees of freedom (DOFs) for displacement, and p is the total number of DOFs associated with pressure. In this formulation, $\boldsymbol{M}$ represents the global mass matrix, $\boldsymbol{D}$ the damping matrix, $\boldsymbol{K}$ the global stiffness matrix, and $\boldsymbol{Q}$ the coupling matrix linking displacement and pressure fields. The vectors $\boldsymbol{F}_{\boldsymbol{ext}}$ and $\boldsymbol{F}_{\boldsymbol{int}}$ represent the external and internal force vectors, respectively. The individual matrices are defined as follows:

$$\boldsymbol{M} = \int_{\Omega} (\boldsymbol{N}_u)^T \rho \boldsymbol{N}_u d\Omega$$

$$\boldsymbol{K} = \int_{\Omega} (\nabla^s \boldsymbol{N}_u)^T \mathbb{D} \boldsymbol{B}_u d\Omega$$

https://doi.org/10.5194/egusphere-2026-1658
Preprint. Discussion started: 20 April 2026

$$\boldsymbol{D} = a_{Ray}\boldsymbol{M} + b_{Ray}\boldsymbol{K} + \int_{\Gamma_w} \boldsymbol{N}_u{}^T \bar{\rho}\boldsymbol{V}\boldsymbol{N}_u d\Gamma \tag{33}$$

$$\boldsymbol{Q} = \int_{\Omega} (\nabla^s \boldsymbol{N}_u)^T \alpha \boldsymbol{m} \boldsymbol{N}_p d\Omega + \int_{\Gamma_d} [\![\boldsymbol{N}_u]\!]^T . \mathbf{n}_{\Gamma_d} \boldsymbol{N}_p d\Gamma$$

$$\boldsymbol{F}_{ext} = \int_{\Omega} (\boldsymbol{N}_u)^T \rho \boldsymbol{b} d\Omega + \int_{\Gamma_t} (\boldsymbol{N}_u)^T \bar{\boldsymbol{t}} d\Gamma$$

$$\boldsymbol{F}_{int} = \int_{\Gamma_d^{\sim}} [\![\boldsymbol{N}_u]\!]^T \left(P_N \mathbf{n}_{\Gamma_d} + P_T \mathbf{t}_{\Gamma_d}\right) d\Gamma$$

where the vector $\mathbf{m} = \{1 \quad 1 \quad 0\}^T$ represents the discrete form of the Dirac delta function, ∇^s is the symmetric gradient operator. The global damping matrix $\boldsymbol{D}$ consists of a combination of Rayleigh damping, introduced to attenuate spurious high-frequency oscillations, here defined as a linear combination of the mass and stiffness matrices (Liu & Gorman, 1995), and a Lysmer–Kuhlemeyer absorbing boundary formulation (Lysmer & Kuhlemeyer, 1969), which is employed to suppress artificial wave reflections at the model boundaries. In this context, a_{Ray} and b_{Ray} are the Rayleigh damping coefficients. These coefficients are determined by prescribing a target damping ratio $\xi = 0.04$ at two natural angular frequencies ω_1 and ω_3, defined as (Kontoe et al., 2011):

$$a_{Ray} = \frac{2\omega_1\omega_3\xi}{\omega_1+\omega_3}, b_{Ray} = \frac{2\xi}{\omega_1+\omega_3} \tag{34}$$

In the second term in damping matrix, the parameter $\bar{\rho}$ denotes the spatially averaged density of the mixture, and $\boldsymbol{V}$ is a velocity-dependent matrix defined as (Lysmer & Kuhlemeyer, 1969):

$$\boldsymbol{V} = \begin{cases} \begin{bmatrix} a_p \bar{V}_p & 0 \\ 0 & a_s \bar{V}_s \end{bmatrix}, & \text{if } \boldsymbol{n}_\Gamma \| x \\ \begin{bmatrix} a_s \bar{V}_s & 0 \\ 0 & a_p \bar{V}_p \end{bmatrix}, & \text{if } \boldsymbol{n}_\Gamma \| y \end{cases} \tag{35}$$

where a_p and a_s are scaling coefficients, here both taken equal to unity, and $\bar{V}_p$ and $\bar{V}_s$ are the average compressional and shear velocities. For the pressure field, the semi-discrete governing equation can be written as:

$$\boldsymbol{C}_{p\times l}\dot{\boldsymbol{U}}_{l\times 1} + \boldsymbol{Q}^p{}_{p\times l}\dot{\boldsymbol{U}}_{l\times 1} + \boldsymbol{H}_{p\times p}\boldsymbol{P}_{p\times 1} + \boldsymbol{S}_{p\times p}\dot{\boldsymbol{P}}_{p\times 1} - \boldsymbol{q}_{ext} = 0 \tag{36}$$

where $\boldsymbol{C}$ represents the inertial coupling between the fluid and the solid skeleton, $\boldsymbol{H}$ is the hydraulic conductivity matrix, $\boldsymbol{S}$ denotes the storage matrix, and $\boldsymbol{q}_{ext}$ is an external source term. These matrices are defined as follows:

$$\boldsymbol{C} = \int_{\Omega} \left(\nabla \boldsymbol{N}_p\right)^T \boldsymbol{k} \cdot \rho_f \boldsymbol{N}_p d\Omega$$

$$\boldsymbol{H} = \int_{\Omega} \left(\nabla \boldsymbol{N}_p\right)^T \boldsymbol{k} \left(\nabla \boldsymbol{N}_p\right) d\Omega + \int_{\Gamma_d} \left(\nabla \boldsymbol{N}_p\right)^T . \mathbf{t}_{\Gamma_d} \left(\frac{w^3}{12\mu_f}\right) \left(\nabla \boldsymbol{N}_p\right) . \mathbf{t}_{\Gamma_d} d\Gamma$$

$$\boldsymbol{S} = \int_{\Omega} \left(\boldsymbol{N}_p\right)^T S_s \boldsymbol{N}_p d\Omega + \int_{\Gamma_d} \left(\boldsymbol{N}_p\right)^T w C_f \boldsymbol{N}_p d\Gamma \tag{37}$$

$$\boldsymbol{Q}^p = \boldsymbol{Q}^T + \int_{\Gamma_d} \left(\boldsymbol{N}_p\right)^T w \, \mathbf{t}_{\Gamma_d} . \langle \nabla^s \boldsymbol{N}_u \rangle . \mathbf{t}_{\Gamma_d} d\Gamma$$

$$\boldsymbol{q}_{ext} = \int_{\Omega} \left(\nabla \boldsymbol{N}_p\right)^T \boldsymbol{k} \rho_f \mathbf{b} d\Omega - \int_{\Gamma_w} \left(\boldsymbol{N}_p\right)^T \bar{q} d\Gamma - \int_{\Gamma_d} \left(\nabla \boldsymbol{N}_p\right)^T . \mathbf{t}_{\Gamma_d} \left(\frac{w^3}{12\mu_f}\right) \rho_f \mathbf{b} . \mathbf{t}_{\Gamma_d} d\Gamma$$

2.5.1 Fully implicit time integration strategy

The semi-discrete XFEM governing equations are first integrated over time using a fully implicit solution approach, which functions as the reference formulation throughout this work. Displacement is advanced with a generalized Newmark GN22 method, while pressure is updated with a GN11 scheme. These methods ensure stable and accurate integration of second-order

https://doi.org/10.5194/egusphere-2026-1658
Preprint. Discussion started: 20 April 2026

and first-order time-dependent equations respectively. The unknown fields at time $t_{n+1} = t_n + \Delta t$ are related to known values at t_n through the following formulas:

$$\begin{aligned}
\ddot{\boldsymbol{U}}_{n+1} &= \tfrac{1}{\beta\Delta t^2}(\boldsymbol{U}_{n+1} - \boldsymbol{U}_n) - \tfrac{1}{\beta\Delta t}\dot{\boldsymbol{U}}_n - \left(\tfrac{1}{2\beta} - 1\right)\ddot{\boldsymbol{U}}_n \\
\dot{\boldsymbol{U}}_{n+1} &= \tfrac{\gamma}{\beta\Delta t}(\boldsymbol{U}_{n+1} - \boldsymbol{U}_n) - \left(\tfrac{\gamma}{\beta} - 1\right)\dot{\boldsymbol{U}}_n - \Delta t\left(\tfrac{\gamma}{2\beta} - 1\right)\ddot{\boldsymbol{U}}_n \\
\dot{\boldsymbol{P}}_{n+1} &= \tfrac{1}{\Delta t}(\boldsymbol{P}_{n+1} - \boldsymbol{P}_n)
\end{aligned} \tag{38}$$

Unconditional stability of the displacement integration is ensured by selecting Newmark parameters satisfying $\gamma \geq 0.5, \beta \geq 0.25(0.5+\gamma)^2$. In this work, the constant-average-acceleration scheme is employed with $\gamma = 0.5$ and $\beta = 0.25$ (Newmark, 1959). The vectors $\boldsymbol{U}_n$, $\dot{\boldsymbol{U}}_n$, and $\ddot{\boldsymbol{U}}_n$ denote the displacement, velocity, and acceleration fields— including both standard and enriched degrees of freedom—at time step n, while $\boldsymbol{P}_n$ represents the corresponding pressure field. Substitution of the time discretization into the semi-discrete equations yields a fully discrete nonlinear system at $n+1$ is formulated. The residual form of the coupled system is written as (Khoei, 2015):

$$\begin{aligned}
\boldsymbol{R}_{U_{n+1}} &= \left(\tfrac{1}{\beta\Delta t^2}\boldsymbol{M} + \tfrac{\gamma}{\beta\Delta t}\boldsymbol{D} + \boldsymbol{K}\right)\boldsymbol{U}_{n+1} - \boldsymbol{Q}\boldsymbol{P}_{n+1} - \left(\tfrac{1}{\beta\Delta t^2}\boldsymbol{M} + \tfrac{1}{\beta\Delta t^2}\boldsymbol{D}\right)\boldsymbol{U}_n \\
&- \left(\tfrac{1}{\beta\Delta t}\boldsymbol{M} + \tfrac{1}{\beta\Delta t}\boldsymbol{D}\right)\dot{\boldsymbol{U}}_n - \left(\left(\tfrac{1}{2\beta} - 1\right)\boldsymbol{M} + \left(\tfrac{1}{2\beta} - 1\right)\boldsymbol{D}\right)\ddot{\boldsymbol{U}}_n + \boldsymbol{F}_{\boldsymbol{int}} - \boldsymbol{F}_{\boldsymbol{ext}} = \boldsymbol{0}
\end{aligned} \tag{39}$$

$$\begin{aligned}
\boldsymbol{R}_{P_{n+1}} &= \left(\tfrac{1}{\beta\Delta t^2}\boldsymbol{C} + \tfrac{\gamma}{\beta\Delta t}\boldsymbol{Q}^p{}_{n+1}\right)\boldsymbol{U}_{n+1} + \left(\boldsymbol{H}_{n+1} + \tfrac{1}{\theta\Delta t}\boldsymbol{S}_{\boldsymbol{n+1}}\right)\boldsymbol{P}_{n+1} - \left(\tfrac{1}{\theta\Delta t}\boldsymbol{S}_{\boldsymbol{n+1}}\right)\boldsymbol{P}_n \\
&- \left(\tfrac{1}{\beta\Delta t^2}\boldsymbol{C} + \tfrac{\gamma}{\beta\Delta t}\boldsymbol{Q}^p{}_{n+1}\right)\boldsymbol{U}_n - \left(\tfrac{1}{\beta\Delta t}\boldsymbol{C} + \left(\tfrac{\gamma}{\beta} - 1\right)\boldsymbol{Q}^p{}_{n+1}\right)\dot{\boldsymbol{U}}_n \\
&- \left(\left(\tfrac{1}{2\beta} - 1\right)\boldsymbol{C} + \Delta t\left(\tfrac{\gamma}{2\beta} - 1\right)\boldsymbol{Q}^p{}_{n+1}\right)\ddot{\boldsymbol{U}}_n - \boldsymbol{q}_{\boldsymbol{ext}} = \boldsymbol{0}
\end{aligned} \tag{40}$$

The resulting coupled nonlinear system is solved using a fully monolithic Newton–Raphson approach, in which displacement and pressure unknowns are updated simultaneously at each time step. At iteration k of time step $n+1$, the residual equations are linearized about the current solution estimate, leading to the following incremental system:

$$\boldsymbol{J}\left(\boldsymbol{U}_{n+1}{}^k, \boldsymbol{P}_{n+1}{}^k\right)\begin{Bmatrix}\delta\boldsymbol{U}_{n+1}{}^{k+1} \\ \delta\boldsymbol{P}_{n+1}{}^{k+1}\end{Bmatrix} = -\begin{Bmatrix}\boldsymbol{R}_{U_{n+1}}{}^k \\ \boldsymbol{R}_{P_{n+1}}{}^k\end{Bmatrix} \tag{41}$$

where $\boldsymbol{J}$ is the Jacobian matrix evaluated at the current iteration. The Jacobian has a block structure and is given by:

$$\boldsymbol{J}\left(\boldsymbol{U}_{n+1}{}^k, \boldsymbol{P}_{n+1}{}^k\right) = \begin{bmatrix}\frac{\partial \boldsymbol{R}_{U_{n+1}}{}^k}{\partial \boldsymbol{U}} & \frac{\partial \boldsymbol{R}_{U_{n+1}}{}^k}{\partial \boldsymbol{P}} \\ \frac{\partial \boldsymbol{R}_{P_{n+1}}{}^k}{\partial \boldsymbol{U}} & \frac{\partial \boldsymbol{R}_{P_{n+1}}{}^k}{\partial \boldsymbol{P}}\end{bmatrix} = \begin{bmatrix}\frac{1}{\beta\Delta t^2}\boldsymbol{M} + \frac{\gamma}{\beta\Delta t}\boldsymbol{D} + \boldsymbol{K} + \frac{\partial \boldsymbol{F}_{\boldsymbol{int}}}{\partial \boldsymbol{U}} & -\boldsymbol{Q} \\ \frac{1}{\beta\Delta t^2}\boldsymbol{C} + \frac{\gamma}{\beta\Delta t}\boldsymbol{Q}^p{}_{n+1} & \boldsymbol{H}_{n+1} + \frac{1}{\Delta t}\boldsymbol{S}_{\boldsymbol{n+1}}\end{bmatrix} \tag{42}$$

Due to the hydro-mechanical coupling terms and the time discretization, the Jacobian matrix is generally non-symmetric. This non-symmetry can increase both memory requirements and computational cost. To improve numerical efficiency, the rows associated with the displacement equations are scaled by the factor $\frac{-\gamma}{\beta\Delta t}$. This operation yields an equivalent system with a more symmetric structure (Khoei, 2015):

$$\boldsymbol{J}\left(\boldsymbol{U}_{n+1}{}^k, \boldsymbol{P}_{n+1}{}^k\right) = \begin{bmatrix}\frac{-\gamma}{\beta\Delta t}\left(\frac{1}{\beta\Delta t^2}\boldsymbol{M} + \frac{\gamma}{\beta\Delta t}\boldsymbol{D} + \boldsymbol{K} + \frac{\partial \boldsymbol{F}_{\boldsymbol{int}}}{\partial \boldsymbol{U}}\right) & \frac{\gamma}{\beta\Delta t}\boldsymbol{Q} \\ \frac{1}{\beta\Delta t^2}\boldsymbol{C} + \frac{\gamma}{\beta\Delta t}\boldsymbol{Q}^p{}_{n+1} & \boldsymbol{H}_{n+1} + \frac{1}{\Delta t}\boldsymbol{S}_{\boldsymbol{n+1}}\end{bmatrix} \tag{43}$$

https://doi.org/10.5194/egusphere-2026-1658
Preprint. Discussion started: 20 April 2026

The contribution of the interface to the Jacobian matrix arises from the dependence of the internal force vector on displacement discontinuities. Its linearization with respect to the displacement field is expressed as:

$$\frac{\partial \boldsymbol{F_{int}}}{\partial U} = \int_{\widetilde{\Gamma_d}} [\boldsymbol{N}_u]^T \boldsymbol{E} [\boldsymbol{N}_u] d\Gamma \tag{44}$$

where $\boldsymbol{E}$ denotes the algorithmic (consistent) tangent operator associated with the fault constitutive response. This operator depends on the current contact state and is evaluated according to the active regime of the fault, i.e., stick or slip. In the stick regime, the corresponding tangent operator associated with fault-plane plasticity is given by:

$$\boldsymbol{E}^{stick} = \frac{\partial \left(P_N \boldsymbol{n}_{\Gamma_d} + P_T \boldsymbol{t}_{\Gamma_d}\right)}{\partial [\![\boldsymbol{u}]\!]} = \boldsymbol{n}_{\Gamma_d} \otimes \frac{\partial P_N}{\partial [\![\boldsymbol{u}]\!]} + \boldsymbol{t}_{\Gamma_d} \otimes \frac{\partial P_T}{\partial [\![\boldsymbol{u}]\!]} = k_N \left(\boldsymbol{n}_{\Gamma_d} \otimes \boldsymbol{n}_{\Gamma_d}\right) + k_T (\boldsymbol{I} - \boldsymbol{n}_{\Gamma_d} \otimes \boldsymbol{n}_{\Gamma_d}) \tag{45}$$

This expression reflects the linear elastic resistance to tangential motion during the stick phase, where the amount of plastic slip is zero ($\zeta^{n+1} = 0$). Under slipping conditions ($\zeta^{n+1} \neq 0$), the tangential traction, P_T, is governed by a rate-dependent frictional constitutive law. In this case, the linearization of the tangential traction with respect to the displacement jump is required to construct a consistent Jacobian contribution. Under slipping conditions, the derivative of the tangential traction magnitude with respect to the displacement discontinuity is given by (F. Liu & Borja, 2009):

$$\frac{\partial P_T}{\partial [\![\boldsymbol{u}]\!]} = k_T \left(\boldsymbol{t}_{\Gamma_d} - \operatorname{sgn}(P_T) \frac{\partial \zeta}{\partial [\![\boldsymbol{u}]\!]}\right) \tag{46}$$

At a locally converged stress state, the derivative of ζ with respect to the displacement jump can be expressed as:

$$\frac{\partial \zeta}{\partial [\![\boldsymbol{u}]\!]} = \frac{k_T \boldsymbol{t}_{\Gamma_d} + \operatorname{sgn}(P_T) k_N f^{n+1} \boldsymbol{n}_{\Gamma_d}}{\operatorname{sgn}(P_T) k_T - \frac{\partial f}{\partial \zeta} P_N{}^{n+1} \operatorname{sgn}(P_T)} \tag{47}$$

Substituting Eq. (20) into Eq. (47), and inserting the result into the traction derivative yields the consistent linearization of the tangential traction with respect to the displacement jump:

$$\frac{\partial \|P_T\|}{\partial [\![\boldsymbol{u}]\!]} = K_T \left(\boldsymbol{t}_{\Gamma_d} - \frac{k_T \boldsymbol{t}_{\Gamma_d} + \operatorname{sgn}(P_T) k_N f^{n+1} \boldsymbol{n}_{\Gamma_d}}{k_T - \frac{1}{\Delta t}\left(\frac{a}{V^{n+1}} - \frac{b}{\theta^{n+1}} \frac{D_c \Delta t (\theta^{n+1} + \Delta t)}{(D_c + \Delta t V^{n+1})^2}\right) P_N{}^{n+1}} \right) \tag{48}$$

Finally, the consistent algorithmic tangent operator associated with the slipping regime is obtained as:

$$\boldsymbol{E}^{slip} = \boldsymbol{t}_{\Gamma_d} \otimes K_T \left(\boldsymbol{t}_{\Gamma_d} - \frac{k_T \boldsymbol{t}_{\Gamma_d} + \operatorname{sgn}(P_T) k_N f^{n+1} \boldsymbol{n}_{\Gamma_d}}{k_T - \frac{1}{\Delta t}\left(\frac{a}{V^{n+1}} - \frac{b}{\theta^{n+1}} \frac{D_c \Delta t (\theta^{n+1} + \Delta t)}{(D_c + \Delta t V^{n+1})^2}\right) P_N{}^{n+1}} \right) + k_N \left(\boldsymbol{n}_{\Gamma_d} \otimes \boldsymbol{n}_{\Gamma_d}\right) \tag{49}$$

The convergence of the Newton–Raphson solution procedure is evaluated by tracking scaled residual measures associated with the displacement and pore-pressure unknowns. At every iteration, the residual of the mechanical equilibrium equations is normalized with respect to the applied external forces and expressed as

$$Re_{\boldsymbol{U}} = \frac{\|\boldsymbol{R}_{\boldsymbol{U}_{n+1}}\|}{\|\boldsymbol{F}_{\boldsymbol{ext}}\|} \tag{50}$$

while the fluid-flow residual is scaled by the prescribed external flux and written as:

$$Re_{\boldsymbol{P}} = \frac{\|\boldsymbol{R}_{\boldsymbol{P}_{n+1}}\|}{\|\boldsymbol{q}_{\boldsymbol{ext}}\|} \tag{51}$$

https://doi.org/10.5194/egusphere-2026-1658
Preprint. Discussion started: 20 April 2026

To consistently assess convergence across the coupled hydro-mechanical system, a unified error indicator is constructed by combining the normalized residuals into a single Euclidean norm:

$$\|R\| = \sqrt{(Re_U)^2 + (Re_p)^2} \tag{52}$$

Convergence is achieved once this combined measure in iterations drops below a specified tolerance (set here to 10^{-6}). This formulation enforces the simultaneous convergence of both the mechanical and hydraulic subproblems, ensuring that force equilibrium and mass conservation are satisfied with similar accuracy while preventing the preferential convergence of either field.

An adaptive time-stepping scheme is used exclusively within the fully implicit formulation to efficiently handle the quasi-static loading and nucleation phases before dynamic rupture. During stable fault behavior, relatively large time steps are allowed to minimize computational costs. As fault slip accelerates toward nucleation, the time step is automatically decreased to adequately capture the evolving frictional response and stress redistribution. The time increment is defined as:

$$\Delta t = max\{\Delta t_{min}, \Delta t_{evol}\} \tag{53}$$

where Δt_{min} defines a lower bound required to resolve rapid instabilities, and Δt_{evol} is a variable step size controlled by the current fault slip rate defined by (Lapusta & Liu, 2009):

$$\Delta t_{evol} = \xi D_c / V \tag{54}$$

where ξ scales the allowable slip increment per time step and is constrained to remain below a prescribed upper limit to ensure numerical stability and accuracy. In the present two-dimensional simulations, a conservative value of $\xi = 0.1$ is adopted to provide enhanced resolution during rapid fault slip.

2.5.2 Hybrid implicit-explicit (IMEX) approach

While the fully implicit formulation provides a robust and accurate reference solution, its computational cost can become significant during rapid slip episodes and strongly nonlinear frictional response. To address this limitation, we here introduce a hybrid implicit–explicit time integration strategy that builds directly on the fully implicit framework described above. In the initial stage, the system is advanced using a fully implicit dynamic solver. This regime is maintained until the slip velocity on the fault reaches a prescribed threshold V_{th}. Beyond this point, the formulation switches to a fully explicit dynamic update, initialized using the state variables obtained at the final implicit time step. Given the strong nonlinearity of the problem during dynamic slip, the explicit phase employs a central difference time integration scheme. This method approximates temporal derivatives using staggered evaluations in time, providing an efficient and robust update for velocity and acceleration. The kinematic relations are expressed as (Koutromanos, 2018):

$$\dot{\boldsymbol{U}}_{n+1/2} = \frac{\boldsymbol{U}_{n+1} - \boldsymbol{U}_n}{\Delta t} \rightarrow \boldsymbol{U}_{n+1} = \boldsymbol{U}_n + \Delta t \cdot \dot{\boldsymbol{U}}_{n+1/2} \tag{55}$$

$$\ddot{\boldsymbol{U}}_n = \frac{\dot{\boldsymbol{U}}_{n+1/2} - \dot{\boldsymbol{U}}_{n-1/2}}{\Delta t} \rightarrow \dot{\boldsymbol{U}}_{n+1/2} = \dot{\boldsymbol{U}}_{n-1/2} + \Delta t \cdot \ddot{\boldsymbol{U}}_n \tag{56}$$

The equation of motion is enforced at the discrete time step n. Assuming that displacement $\boldsymbol{U}_n$, velocity $\dot{\boldsymbol{U}}_{n-1/2}$, and pressure $\boldsymbol{P}_n$, are known from the previous time step, the acceleration is obtained from:

$$\left(\boldsymbol{M} + \frac{\Delta t}{2}\boldsymbol{D}\right)\ddot{\boldsymbol{U}}_n = \boldsymbol{F_{ext}} - \boldsymbol{F_{int}} - \boldsymbol{D}\dot{\boldsymbol{U}}_{n-1/2} - \boldsymbol{K}\boldsymbol{U}_n + \boldsymbol{U}_n\boldsymbol{P}_n \tag{57}$$

https://doi.org/10.5194/egusphere-2026-1658
Preprint. Discussion started: 20 April 2026

Since all terms appearing on the right-hand side of Eq. (57) are known at time level n, the nodal displacement $\ddot{\boldsymbol{U}}_n$ can be directly evaluated. Once the acceleration is obtained, the velocity is advanced using Eq. (56), followed by the update of the displacement field through Eq. (55). With the displacement at time step $n+1$ available, the normal gap is computed according to Eq. (8), allowing the fracture aperture to be updated accordingly. The pressure field is then advanced in time using a backward Euler discretization, yielding:

$$(\boldsymbol{S_{n+1}} + \Delta t \boldsymbol{H}_{n+1})\boldsymbol{P}_{n+1} = \boldsymbol{q_{ext}} - \boldsymbol{C}\ddot{\boldsymbol{U}}_n - \boldsymbol{Q}^{p}{}_{n+1}\dot{\boldsymbol{U}}_{n+1/2} \tag{58}$$

Numerical stability during the explicit phase is ensured by enforcing a time-step restriction based on the Courant–Friedrichs–Lewy (CFL) condition, which requires that wave propagation within a single time increment does not exceed the characteristic size of a finite element. The critical time step is therefore estimated as (Koutromanos, 2018):

$$\Delta t_{cr} = 0.5 \cdot min\left(\sqrt{\frac{\rho^e}{E^e}}\, l^e\right) \tag{59}$$

where l^e denotes the characteristic element length, taken as the square root of the element area, and E^e is Young's modulus of the element. The explicit dynamic formulation is applied as long as the slip velocity on at least one fault element exceeds the prescribed threshold value V_{th}. Once the slip velocities across all fault elements fall below this threshold, the solution strategy reverts to the fully implicit dynamic formulation. A detailed flowchart illustrating how the adaptive IMEX solution strategy operates is shown in Figure 3.

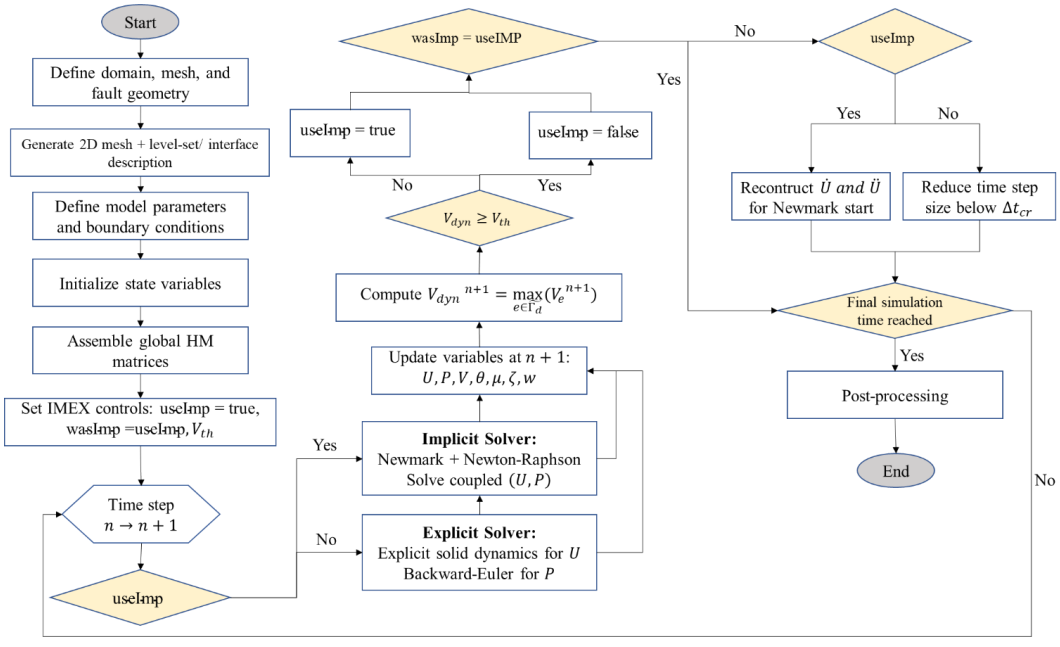

Figure 3: Schematic overview of the adaptive IMEX solution strategy. The model alternates between implicit and explicit solvers based on the fault slip-rate criterion $V_{dyn} \geq V_{th}$, allowing stable treatment of quasi-static deformation and efficient resolution of dynamic rupture.

2.6 Variation of fault permeability due to fault aperture change

Directly using the mechanically computed normal gap to update the hydraulic aperture leads to complete fault closure under compressive normal stress, which is inconsistent with natural faults that retain residual permeability due to surface asperities. To account for this behavior, we relate the hydraulic aperture to the effective normal stress through a constitutive closure law

https://doi.org/10.5194/egusphere-2026-1658
Preprint. Discussion started: 20 April 2026

that represents asperity deformation. In this study, the hydraulic aperture is defined using a piecewise relation (Sabah et al., 2026):

$$w = \begin{cases} w_0 + \frac{P_N D_{n-max}}{k_N D_{n-max} + P_N}, & P_N < 0 \\ g_N, & P_N \geq 0 \end{cases} \quad (60)$$

where w_0 is initial aperture, D_{n-max} is the maximum normal displacement under compressive normal stress, and k_N is initial normal stiffness of the fault. Under compressive normal stress ($P_N < 0$), aperture evolution follows the Barton–Bandis joint-closure model (Bandis et al., 1983), which introduces a stress-dependent lower bound and prevents nonphysical negative apertures. Under zero or tensile normal stress ($P_N \geq 0$), contact is inactive and the aperture is set equal to the mechanical normal gap obtained from the displacement jump across the interface. This formulation ensures a smooth and physically consistent transition between closure and opening regimes.

The resulting aperture is used to update fault permeability via the cubic law and is incorporated into the hydraulic conductance matrix at both solution strategies, enabling realistic simulation of stress-dependent fault transmissivity during fluid injection and reactivation.

3 Verification and model setup

The fully implicit hydromechanical formulation employed in this study has been previously verified and validated in detail in Sabah et al. (2026). That work included comprehensive verification against analytical solutions for saturated porous media (Wang, 2000), as well as established numerical benchmarks for fractured porous systems (Damirchi et al., 2022), in addition to validation using the SEAS (Sequences of Earthquakes and Aseismic Slip) benchmark for rupture dynamics (Erickson et al., 2020). In the present study, the fully implicit formulation is adopted with modifications in enforcing contact constraints and serves as the reference solver. Building upon this verified framework, the extended hybrid IMEX formulation is introduced and its behavior is systematically compared against the fully implicit reference in terms of fault response and numerical performance.

The computational domain is a square region measuring 400 m × 400 m, representing a horizontal cross-section of a fractured reservoir subjected to anisotropic in-situ stresses. As illustrated in Figure 4, a single pre-existing fault cuts across the domain at 45°, extending from (100 m, 101 m) to (300 m, 301 m). A fluid injection well is positioned near the fault center at (220 m, 180 m) to promote fault activation through pore-pressure diffusion and poroelastic stress redistribution.

All boundaries are mechanically constrained: the left and right boundaries are fixed in the x-direction, while displacements along the bottom and top boundaries are constrained in the y-direction. Uniform compressive in-situ stresses are applied within the domain, with $\sigma_x = 60$ MPa and $\sigma_y = 20$ MPa, representing a critically stressed fault with an initial frictional strength of $f = 0.6$. The pore pressure boundary condition is set to $P = 0$ MPa (drained condition) along the right edge, while the remaining boundaries are hydraulically impermeable. The initial pore pressure throughout the domain is set to $P_0 = 0$ MPa.

Fluid injection is initiated at a constant rate of $5 \times 10^{-4}\ m^3(s.m)^{-1}$ from the injection well at $t = 0$ s and continues throughout the simulation period (36 h). This injection induces a progressive increase in pore pressure and associated poroelastic deformation in the vicinity of the fault. The entire domain is discretized using 40,000 bilinear quadrilateral elements (200 × 200 mesh). Rock, fault, and fluid properties are summarized in Table 1.

https://doi.org/10.5194/egusphere-2026-1658
Preprint. Discussion started: 20 April 2026

Table 1. Material properties

Type	Parameter	Value
Rock mass	Poisson's ratio	0.3
	Young's modulus (GPa)	50
	Intrinsic permeability (m^2)	2×10^{-15}
	Biot coefficient	0.75
	Rock density (kg/m^3)	2500
	Porosity	0.1
Injection fluid	Fluid density (kg/m^3)	1000
	Fluid viscosity (Pa s)	0.001
Fault	Reference friction coefficient	0.6
	Characteristic distance (mm)	0.1
	Rate-and-state parameters	$a = 0.01$, $b = 0.02$
	Initial normal stiffness (GPa/m)	20
	Initial shear stiffness (GPa/m)	20
	Initial aperture (mm)	1

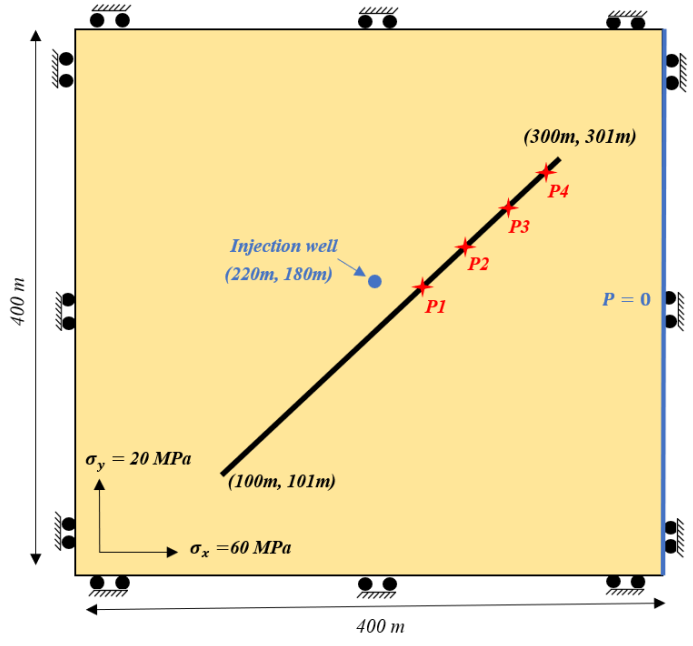

Figure 4: Schematic of a single-phase fluid injection scenario in a homogeneous porous formation containing a fault. The injection well is located at coordinates (220 m, 180 m), and the fault spans from (100 m, 101 m) to (300 m, 301 m). Five observation points along the upper part of the fault (denoted P1–P4) are used to monitor fault response. The reservoir is subjected to anisotropic in-situ **compressive stresses of $\sigma_x = 60$ MPa and $\sigma_y = 20$ MPa, applied as initial stress conditions throughout the domain rather than as boundary tractions. All external boundaries are mechanically constrained by** roller boundary conditions**, allowing tangential displacement while preventing normal motion. The pore-pressure boundary condition is set to $P = 0$ MPa (drained condition) along the right boundary, while the remaining boundaries are hydraulically impermeable.**

4 Results and discussion

4.1 Fully implicit solution

This section examines adaptive time stepping within the implicit solution framework using three different minimum time-step sizes: 0.001 s, 0.0001 s, and 0.00001 s. The minimum time step is the lower limit below which the adaptive algorithm cannot further reduce the time increment. This analysis is motivated by the fact that, although implicit schemes are unconditionally stable, their accuracy—especially during rupture nucleation and dynamic propagation—strongly depends on temporal resolution.

https://doi.org/10.5194/egusphere-2026-1658
Preprint. Discussion started: 20 April 2026

Figure 5 shows the simulation results for three different minimum time-step sizes. The right column represents 0.001 s, the middle column 0.0001 s, and the left column 0.00001 s. The results suggest that a minimum time step of 0.001 s does not provide enough temporal resolution during the dynamic rupture phase. In contrast, decreasing the minimum time step to 0.0001 s and 0.00001 s results in more slip accumulation, higher peak slip rates, and earlier end of the seismic phase. Despite these variations, the upper and lower limits of the friction coefficient and shear stress stay mostly the same across all three cases.

Figure 6 compares different approaches in terms of average slip, seismic moment, moment magnitude, and rupture speed normalized by shear wave velocity. Larger minimum time-step sizes lead to lower average slip, smaller seismic moments, and reduced rupture speed (Fig. 6a, c-d). However, the differences in moment magnitude are relatively small due to its logarithmic nature (Fig. 6-b). The results with minimum time steps of 0.0001 s and 0.00001 s are similar, indicating that 0.0001 s offers an optimal balance between numerical accuracy and computational efficiency. Although slight variations in nucleation time are observed among the three time-step sizes, these differences are on the order of milliseconds and are thus negligible compared to the overall simulation timescale.

For the chosen material properties, the critical time step derived from the CFL condition (Eq. 59) is about 0.00035 s. This shows that, even with adaptive time stepping in an implicit solution framework, the smallest time step needed to properly capture rupture propagation is roughly the same as the critical time step set by stability limits in an explicit approach.

https://doi.org/10.5194/egusphere-2026-1658
Preprint. Discussion started: 20 April 2026

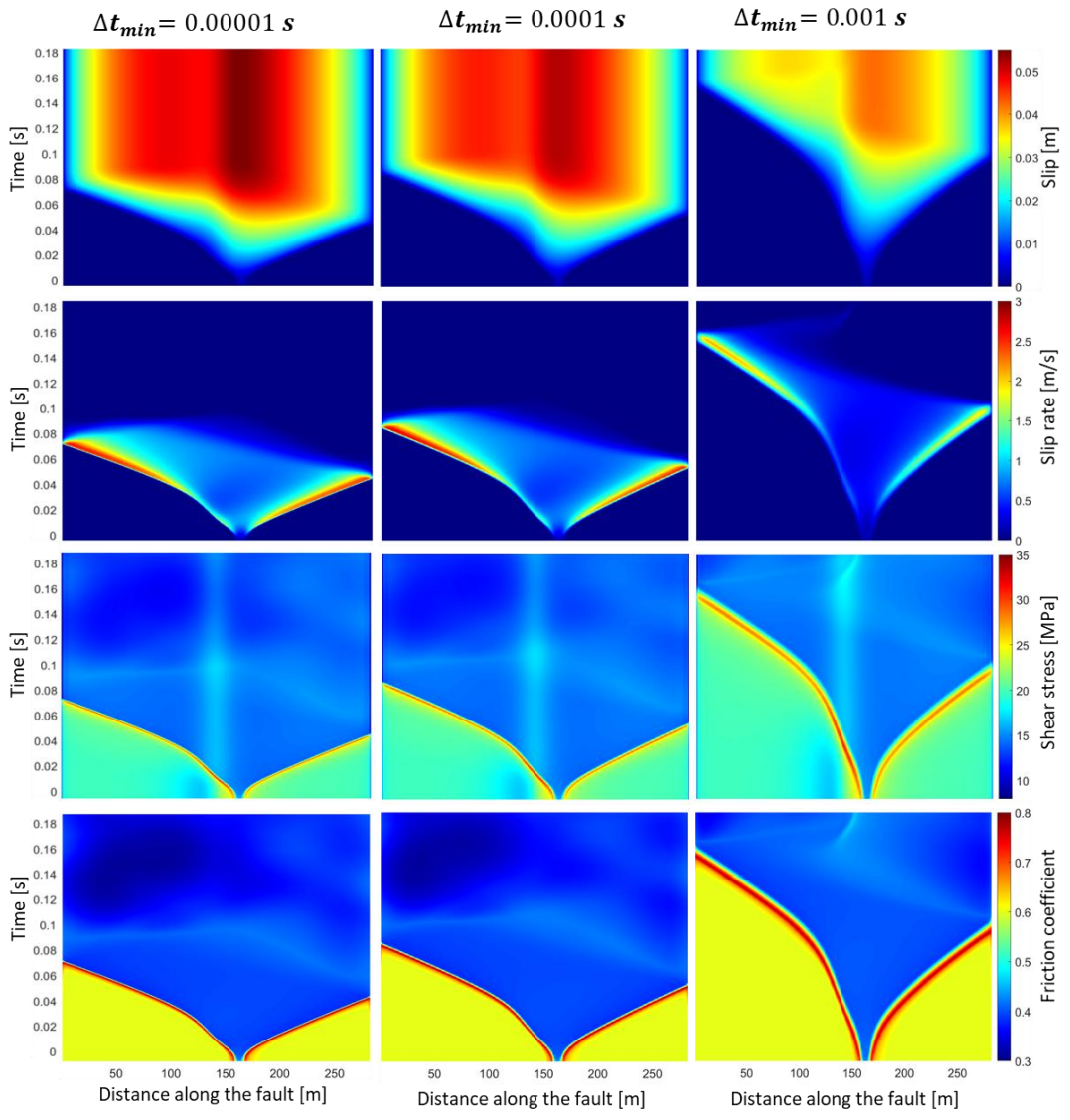

Figure 5: Space–time evolution of fault slip, slip rate, shear stress, and friction coefficient for three minimum time-step sizes: $\Delta t_{min} = 0.00001\ s$ (left), $\Delta t_{min} = 0.0001\ s$ (middle), and $\Delta t_{min} = 0.001\ s$ (right). The time axis in all panels is shifted such that $t = 0$ corresponds to the instant when the maximum slip velocity on the fault first exceeds 0.1m/s. The results highlight the influence of temporal resolution on rupture nucleation and the subsequent dynamic fault response.

https://doi.org/10.5194/egusphere-2026-1658
Preprint. Discussion started: 20 April 2026

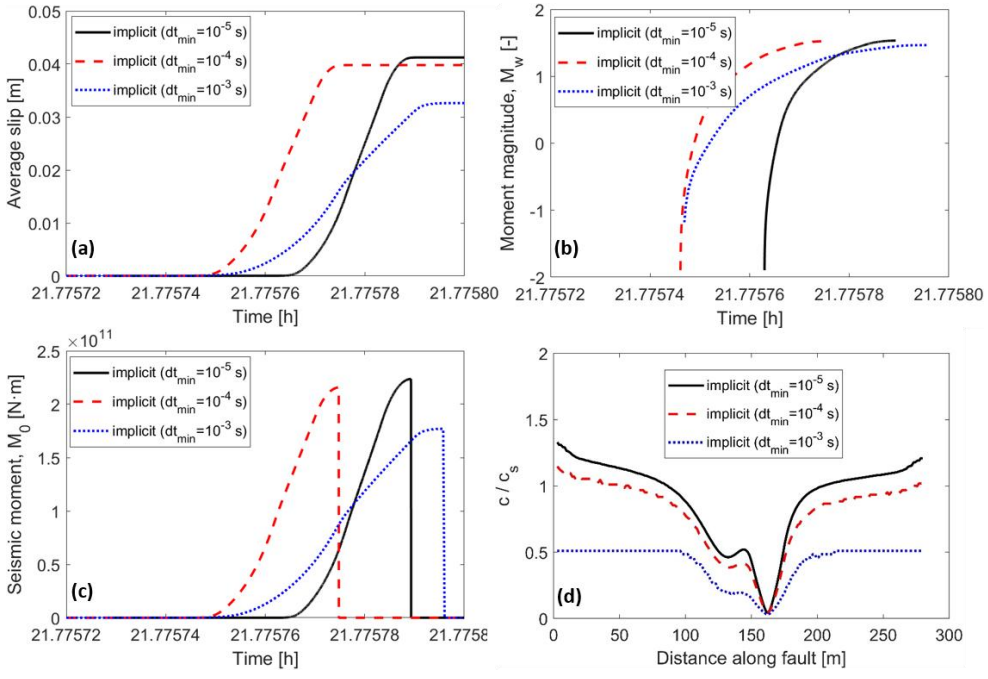

Figure 6: Influence of the minimum time-step size on event evolution for fully implicit simulations. Shown are the time histories of average fault slip (a), moment magnitude (b), seismic moment (c), and the spatial distribution of rupture speed normalized by the shear-wave velocity (d) for $\Delta t_{min} = 0.00001$ s, $\Delta t_{min} = 0.0001$ s, and $\Delta t_{min} = 0.001$ s. In panels (a–c), time is measured from the start of fluid injection. Differences highlight the sensitivity of rupture timing and magnitude estimates to temporal resolution during dynamic instability.

4.2 Hybrid implicit-explicit (IMEX) approach

In the proposed solution strategy, the implicit solver efficiently resolves the quasi-static and nucleation phases, while the explicit solver captures the ensuing dynamic fault slip and rupture propagation in a computationally efficient manner. The transition between implicit and explicit solvers is controlled by a maximum slip-velocity threshold attained on any fault element. An important practical question is therefore the choice of an optimal slip-velocity threshold that minimizes the total computational cost without degrading numerical accuracy.

To assess the computational efficiency of the proposed hybrid IMEX time-integration strategy, we report the total CPU time required to complete each simulation and compare it with the corresponding fully implicit solution. In the fully implicit approach, a minimum time step of $\Delta t_{min} = 0.0001$ s is prescribed; below this value, the adaptive time-stepping scheme does not further reduce the time step during the seismic phase. For the IMEX approach, the same minimum time step of $\Delta t_{min} = 0.0001$ s was used, which is smaller than the maximum allowable value imposed by the CFL condition ($\Delta t_{cr} = 0.00035$ s).

Figure 7 shows that the hybrid strategy consistently reduces the computational cost relative to the fully implicit approach, with CPU-time reductions of approximately 58–71%, depending on the selected slip-velocity threshold V_{th}. The threshold is varied within the range $V_{th} \in [5 \times 10^{-4}, 10^{-1}]$ m/s. Below this range, the explicit phase is activated too early and therefore dominates the overall runtime, making the hybrid approach inefficient. Conversely, for thresholds above this range, the contribution of the explicit solver to the total computational efficiency diminishes; as observed for $V_{th} > 0.1$ m/s, the relative CPU-time reduction no longer improves and begins to decrease. The largest computational savings are obtained for intermediate thresholds, with a maximum reduction of about 71% at $V_{th} = 0.01$ m/s, indicating an optimal balance between implicit and explicit solver contributions.

https://doi.org/10.5194/egusphere-2026-1658
Preprint. Discussion started: 20 April 2026

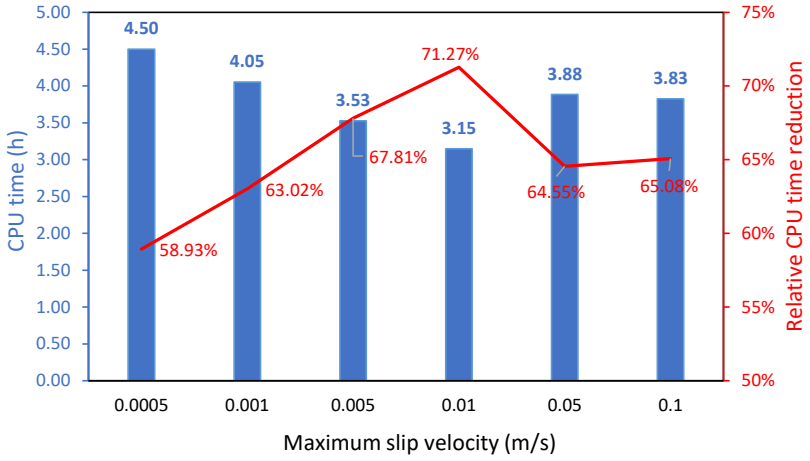

Figure 7: Computational performance of the hybrid IMEX strategy as a function of slip-velocity threshold used to switch solvers. Shown are the total CPU time (blue bars) and the corresponding CPU-time reduction relative to a fully implicit simulation (red line).

Figure 8 compares the temporal evolution of the fault response at four observation points along the fault (P1–P4) obtained using the fully implicit and hybrid IMEX solution strategies. In the IMEX simulations, the transition from implicit to explicit time integration is triggered when the local slip velocity at any fault element exceeds 0.01 m/s.

The slip-rate histories (Fig. 8a) show that both approaches capture the onset, propagation, and overall sequence of dynamic rupture consistently across all observation points. The primary differences between the two approaches are confined to the peak slip velocities, which are slightly higher in the fully implicit simulations. Despite these differences, the timing of rupture arrival and the relative ordering of peak slip rates along the fault remain consistent. The corresponding shear stress evolution (Fig. 8b) exhibits similar stress accumulation prior to instability and rapid stress drop during rupture for both schemes, indicating that the IMEX transition does not introduce spurious stress artifacts. The accumulated slip (Fig. 8c) demonstrates close agreement between the two approaches, with final slip magnitudes at all observation points remaining consistent despite the different integration schemes. Similarly, the evolution of Coulomb failure stress (ΔCFS) (Fig. 8-d) shows comparable timing and amplitude of instability, confirming that the IMEX strategy reproduces the key failure conditions resolved by the fully implicit solver. The friction coefficient evolution (Fig. 8e) highlights the expected rapid weakening during dynamic slip, followed by post-rupture recovery, with both approaches exhibiting nearly identical trends. Finally, the state variable evolution (Fig. 8f) shows consistent rapid evolution during rupture and gradual post-seismic recovery, indicating that the rate-and-state frictional response is preserved across the IMEX transition.

Overall, the figure demonstrates that the IMEX approach, using a slip-velocity threshold of 0.01 m/s for solver switching, accurately reproduces the spatial and temporal evolution of key fault variables obtained with a fully implicit formulation, while enabling substantial reductions in computational cost.

https://doi.org/10.5194/egusphere-2026-1658
Preprint. Discussion started: 20 April 2026

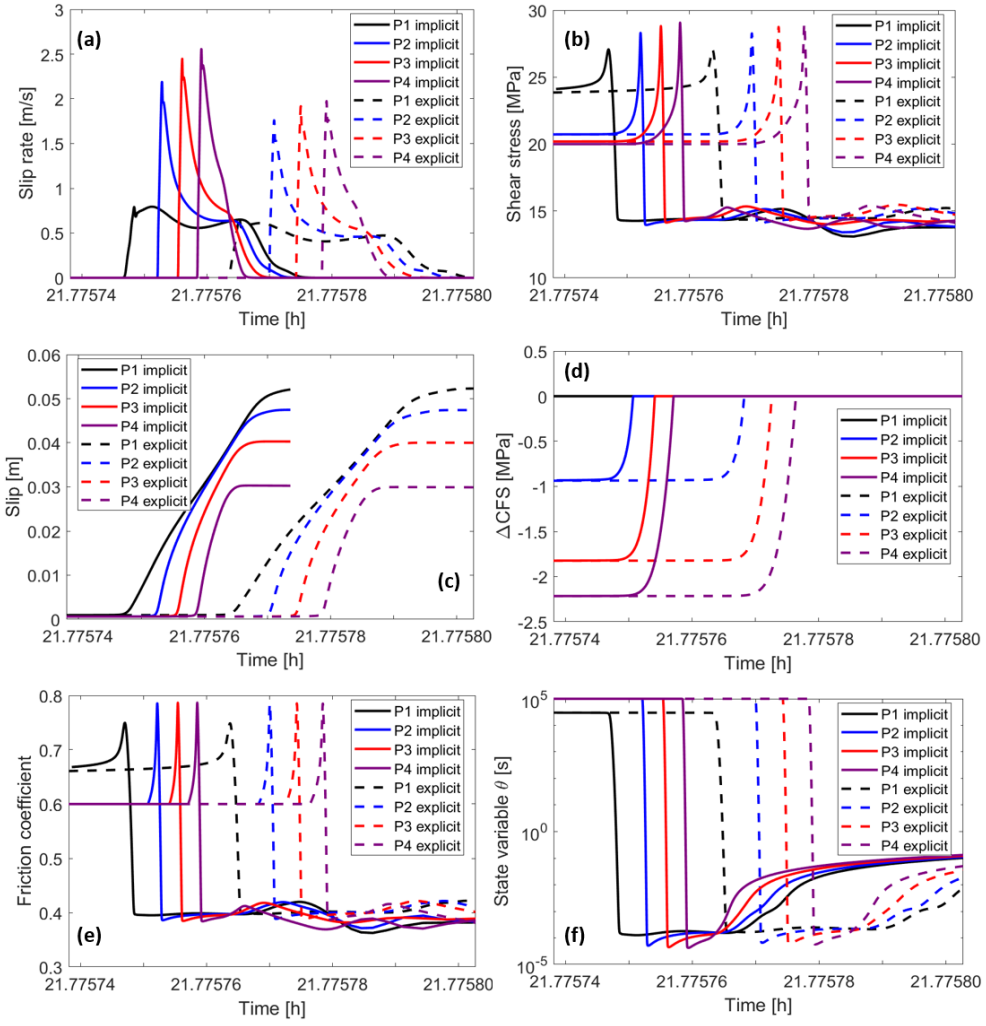

Figure 8: Comparison of fault response at four observation points along the fault (P1–P4) obtained with the fully implicit and hybrid IMEX solution strategies. Shown are the time histories of slip rate (a), shear stress (b), accumulated slip (c), Coulomb failure stress change (d), friction coefficient (e), and state variable (f). Time is measured from the start of fluid injection. Solid lines denote the implicit phase, while dashed lines indicate the explicit phase following the solver switch, triggered when the slip-velocity threshold of 0.01 m/s is exceeded. Both approaches capture the rupture sequence consistently, with minor differences primarily confined to peak slip velocities

Figure 9 compares key event-scale seismicity metrics obtained with the fully implicit solution and the hybrid IMEX approach. The temporal evolution of average slip, moment magnitude, and seismic moment shows that both approaches reproduce the overall rupture evolution and final event size with close agreement (Fig. 9, a-c), with only minor differences in rupture timing. The most pronounced difference is observed in the normalized rupture speed for which the fully implicit solution predicts systematically higher rupture velocities than the IMEX approach (Fig. 9d). This difference increases as the rupture propagates along the fault, reaching approximately 1.3 times higher values at the fault tips. Despite this difference, the spatial pattern of rupture propagation remains consistent between the two methods. Overall, these results indicate that the IMEX formulation preserves the essential characteristics of fault rupture and seismic energy release resolved by the fully implicit solver, while introducing only limited deviations in rupture speed and enabling substantial computational savings.

https://doi.org/10.5194/egusphere-2026-1658
Preprint. Discussion started: 20 April 2026

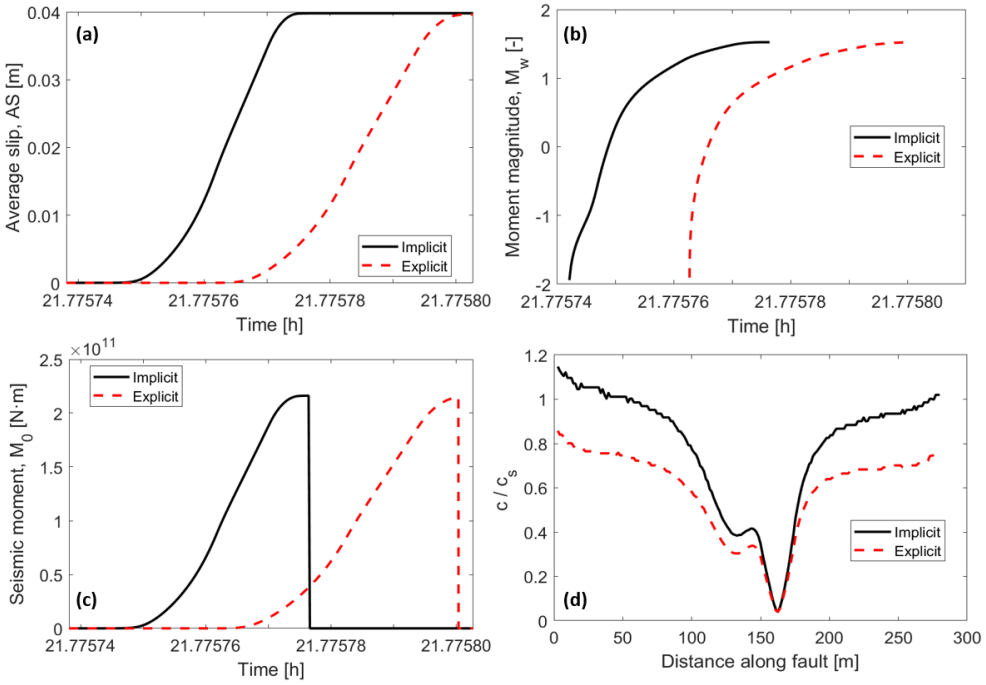

525 **Figure 9: Comparison of event-scale seismicity metrics obtained with the fully implicit and hybrid IMEX solution strategies. Shown are the temporal evolutions of average slip (a), moment magnitude (b), and seismic moment (c), together with the spatial distribution of normalized rupture speed along the fault (d). In panels (a–c), time is measured from the start of fluid injection The IMEX approach reproduces the overall rupture evolution and final event size with only minor differences in timing, while the fully implicit solution predicts systematically higher rupture speeds.**

530 Figure 10 compares the computed synthetic ground-motion evolutions at the location of the injection well obtained with the fully implicit and IMEX approaches. The acceleration time histories (Fig. 10, a-b) show that the IMEX simulations exhibit slightly higher peak accelerations than the fully implicit solution, reflecting the reduced numerical damping associated with explicit integration. In contrast, the velocity records (Fig. 10, c-d) indicate that the fully implicit solution yields higher peak velocities, while the IMEX results remain slightly attenuated. A small delay in wave arrival time is observed for the IMEX

535 simulations relative to the implicit solution, and this delay increases modestly with increasing slip-velocity threshold; however, the absolute timing differences remain negligible. The displacement evolution (Fig. 10, e-f) is nearly identical for all three approaches, with all methods converging to the same final values in both X and Y directions. Overall, these results indicate that the IMEX strategy preserves the essential dynamic response and final deformation while introducing only minor differences in transient wave characteristics.

https://doi.org/10.5194/egusphere-2026-1658
Preprint. Discussion started: 20 April 2026

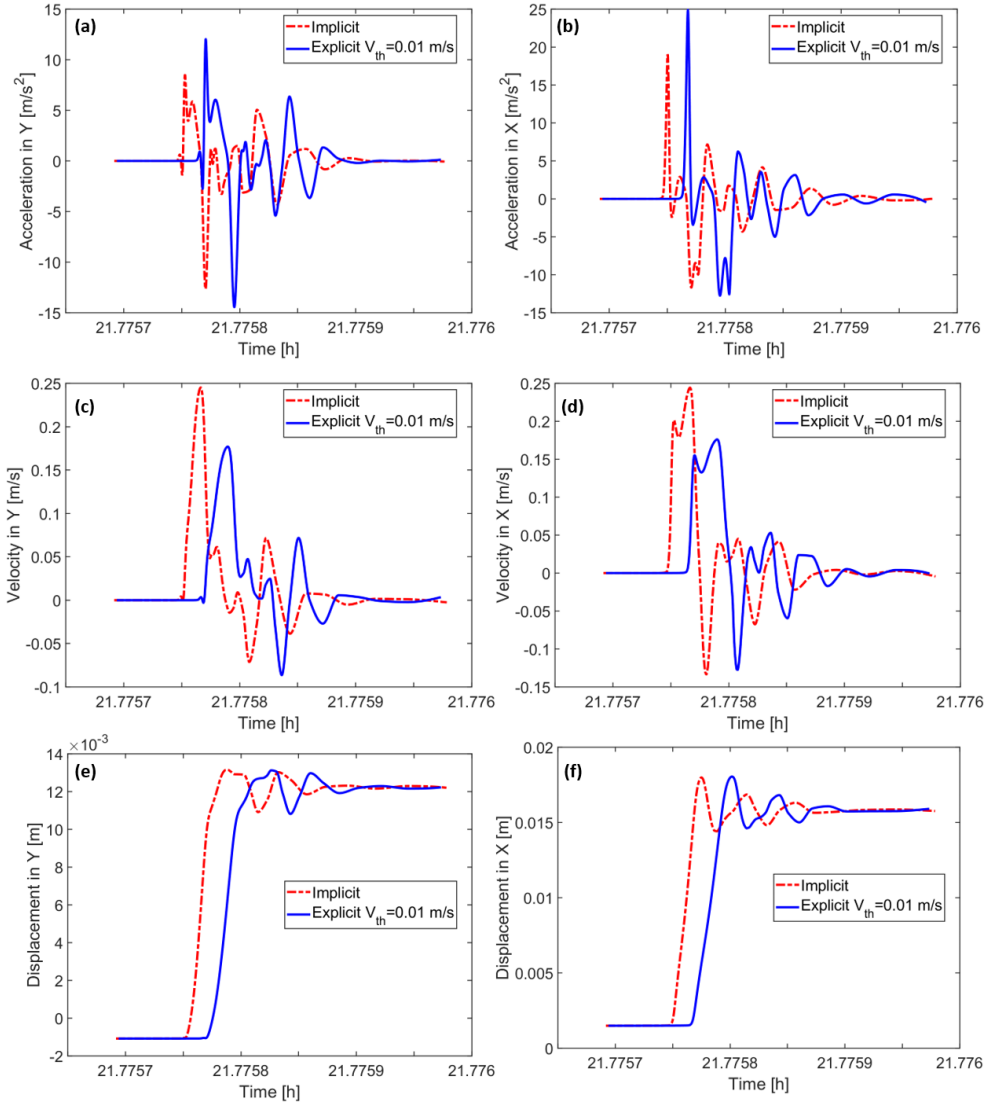

Figure 10: comparison of acceleration, velocity, and displacement time histories obtained with the fully implicit and hybrid IMEX approaches. Time is measured from the start of fluid injection. IMEX simulations exhibit slightly higher peak accelerations, while the implicit solution yields higher peak velocities; all approaches converge to the same final displacement, with only minor delays in wave arrival for IMEX.

5 Conclusion

This study introduced a hybrid IMEX time-integration strategy for simulating injection-induced fault reactivation within a fully coupled hydromechanical XFEM framework. The proposed approach directly addresses the fundamental challenge posed by the extreme separation of time scales inherent to fluid-driven seismicity, ranging from slow reservoir pressurization to rapid fault nucleation and dynamic rupture.

Using a fully implicit poroviscoelasto-dynamic formulation as a reference solution, we demonstrated that although implicit schemes are unconditionally stable, their accuracy during rupture nucleation and propagation is strongly controlled by the minimum time-step size. Insufficient temporal resolution leads to delayed instability, underestimated slip rates, and reduced seismic moments. Our results further showed that the minimum time step required to accurately capture rupture dynamics is

https://doi.org/10.5194/egusphere-2026-1658
Preprint. Discussion started: 20 April 2026

of the same order as the critical time step dictated by the CFL condition, highlighting an intrinsic limitation of purely implicit approaches for dynamic faulting problems.

To overcome this limitation, the proposed IMEX strategy advances the system implicitly during quasi-static loading and nucleation phases, and automatically transitions to an explicit dynamic solver once a prescribed slip-velocity threshold is exceeded. Systematic numerical experiments demonstrated that this adaptive solver switching preserves the accuracy of key fault response metrics, including slip evolution, shear stress, frictional weakening, Coulomb failure stress, and seismic moment, while substantially reducing computational cost. Depending on the selected slip-velocity threshold, the IMEX approach achieved CPU-time reductions of approximately 60–77% relative to the fully implicit formulation, with an optimal balance between efficiency and accuracy obtained for intermediate threshold values.

Comparison of fault-scale and event-scale response revealed that the IMEX formulation reproduces rupture timing, spatial propagation patterns, and final deformation with close agreement to the fully implicit solution. Differences are primarily confined to peak slip velocities and rupture speeds, which are slightly higher in the fully implicit case, reflecting the increased numerical damping associated with implicit integration. Ground-motion comparisons further showed that both approaches converge to identical final displacements, with only minor differences in transient wave characteristics.

An important practical outcome of this study is the demonstration that, within the IMEX framework, omission of the slip tangent operator during the implicit phase does not significantly degrade computational performance or solution accuracy. This finding is particularly relevant for large-scale or three-dimensional simulations, where construction and evaluation of complex frictional Jacobian can become prohibitively expensive.

Overall, the proposed hybrid IMEX XFEM framework provides a robust, efficient, and scalable tool for physics-based simulation of injection-induced seismicity. By combining the stability of implicit integration during slow deformation with the efficiency of explicit dynamics during rupture, the approach enables accurate resolution of multi-scale fault processes at substantially reduced computational cost. Future work will extend the formulation to fully three-dimensional fault networks, by additionally incorporating thermo-hydro-mechanical coupling, and explore its integration into physics-based seismic hazard assessment and adaptive traffic-light systems for subsurface energy operations.

6 Appendices

Appendix A: Effect of slip tangent operator in fully implicit solution approach

From a computational perspective, we compared two time-step sizes ($\Delta t_{min} = 0.0001\ s$ and $\Delta t_{min} = 0.001\ s$) in terms of total CPU time and the number of iterations required for convergence, both with and without inclusion of the slip tangent operator developed section 2.5.1 (Eq. 49). For cases where a balance between computational cost and numerical resolution is required ($\Delta t_{min} = 0.0001\ s$), the fully implicit scheme including the slip tangent operator required 11.87 h of CPU time, whereas omitting the operator increased the runtime to 16.45 h, corresponding to a 28% increase (Fig. A1-a). This indicates that, particularly for three-dimensional simulations and more complex friction laws using small minimum time steps, neglecting the slip tangent operator does not lead to a prohibitive increase in computational cost. In contrast, when computational efficiency is prioritized over temporal resolution ($\Delta t_{min} = 0.001\ s$), omitting the slip tangent operator resulted in an approximately 68% increase in runtime (Fig. A1-b), demonstrating that inclusion of the slip tangent operator is essential for efficient Jacobian assembly in such cases.

https://doi.org/10.5194/egusphere-2026-1658
Preprint. Discussion started: 20 April 2026

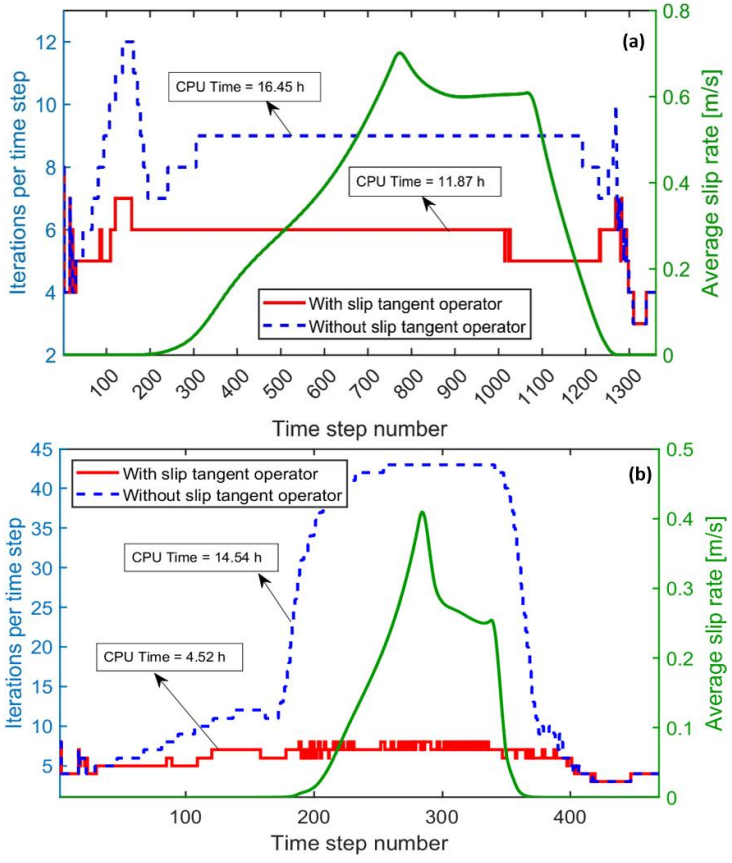

Figure A1: Solver performance with and without the slip tangent operator for two minimum time-step sizes. Shown are the Newton iterations per time step for $\Delta t_{min} = 0.0001$ s (a) and $\Delta t_{min} = 0.001$ s (b), together with the average slip rate. Inclusion of the slip tangent operator reduces iteration counts and total CPU time, with the strongest efficiency gain observed for the larger time step.

For two previous cases, Fig. A2 also compares Newton–Raphson convergence behavior for different slip velocities. The top row (Fig. A2, a-b) corresponds to $\Delta t_{min} = 0.0001\ s$ and the bottom row (Fig. A2, c-d) to $\Delta t_{min} = 0.001\ s$. Results obtained with the slip tangent operator are shown in the left column, while those without the slip tangent operator are shown in the right column. The evolution of the residual norm with iteration number demonstrates that inclusion of the slip tangent operator systematically improves convergence, reducing the number of iterations required to reach a given tolerance, with the effect becoming particularly pronounced for larger time steps and higher slip velocities.

https://doi.org/10.5194/egusphere-2026-1658
Preprint. Discussion started: 20 April 2026

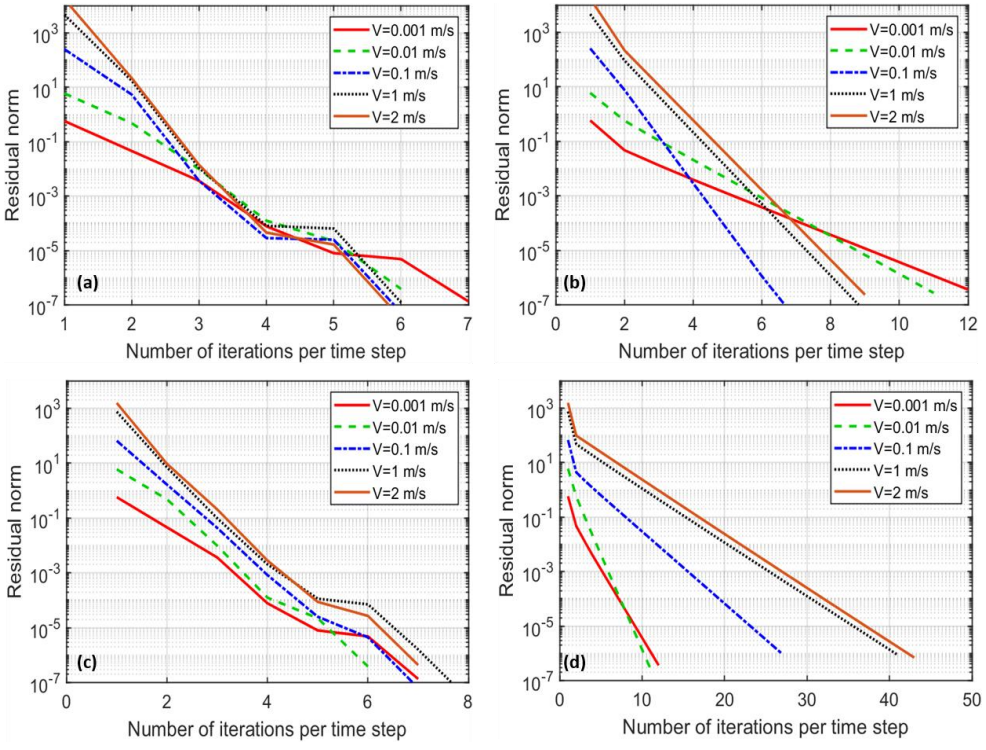

Figure A2: Newton–Raphson convergence behavior for different prescribed slip velocities and two minimum time-step sizes. Panels (a–b) correspond to $\Delta t_{min} = 0.0001$ s, while panels (c–d) correspond to $\Delta t_{min} = 0.001$ s. Results obtained with **the slip tangent operator are shown in the left column, and those** without **the slip tangent operator in the right column. The evolution of the residual norm with iteration number demonstrates that inclusion of the slip tangent operator consistently enhances convergence, reducing the number of iterations required to reach a given tolerance. This improvement becomes increasingly pronounced for larger time steps and higher slip velocities.**

Appendix B: Effect of slip tangent operator in IMEX solution approach

Figure A3 illustrates the computational efficiency of the hybrid IMEX strategy when the slip tangent operator is not included during the implicit phase, for a range of slip-velocity thresholds controlling the solver transition. A minimum time-step size of $\Delta t_{min} = 0.0001$ s is used for the implicit solver and also adopted as the explicit time step. The results show that the highest computational efficiency is achieved for a slip-velocity threshold of 0.01 m/s, yielding a CPU-time reduction of approximately 75%. Comparison with Figure 7 reveals that omitting the slip tangent operator during the implicit phase does not lead to a significant change in overall computational performance. This indicates that, within the IMEX framework, the slip tangent operator may be neglected without compromising efficiency, which is particularly advantageous given the increased complexity associated with its Jacobian evaluation.

https://doi.org/10.5194/egusphere-2026-1658
Preprint. Discussion started: 20 April 2026

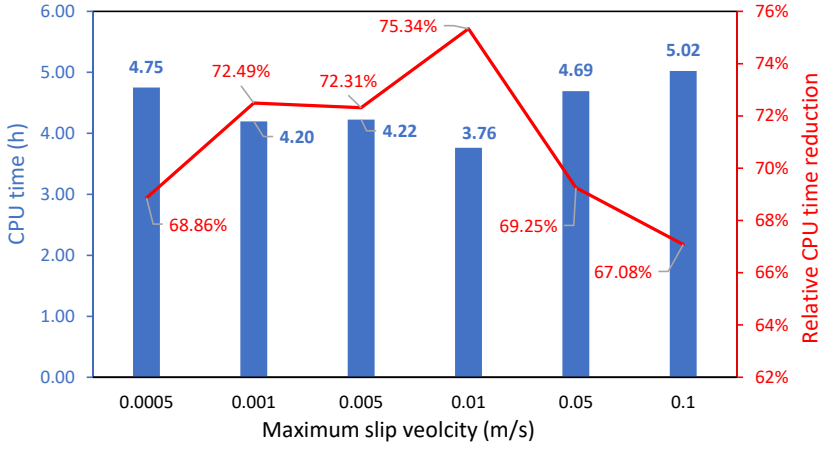

Figure A3: Computational efficiency of the hybrid IMEX approach as a function of the slip-velocity threshold controlling the solver transition. Blue bars indicate the total CPU time, while the red curve shows the relative CPU-time savings compared to the fully implicit solution without including slip tangent operator.

Code availability

The source code used in this study, together with the input files and scripts required to reproduce the results, is publicly available via the following Zenodo repository: https://doi.org/10.5281/zenodo.19220256 (Sabah, 2026). The archived package includes (i) the full simulation/workflow code, (ii) example configuration/input files, and (iii) post-processing scripts for generating the figures and tables reported in this paper. Any additional data generated during the study are either included in the same repository or can be obtained from the corresponding author upon reasonable request.

Author contributions

All authors contributed to the discussion and interpretation of the results and to the review and editing of the manuscript. MS developed the code, designed the methodology, performed the simulations, and prepared the manuscript. MC contributed to the conceptualization and development of the methodology.

Competing interests

At least one of the (co-)authors is a member of the editorial board of Geoscientific Model Development.

Disclaimer

Publisher's note: Copernicus Publications remains neutral with regard to jurisdictional claims made in the text, published maps, institutional affiliations, or any other geographical representation in this paper. While Copernicus Publications makes every effort to include appropriate place names, the final responsibility lies with the authors. Views expressed in the text are those of the authors and do not necessarily reflect the views of the publisher.

https://doi.org/10.5194/egusphere-2026-1658
Preprint. Discussion started: 20 April 2026

Acknowledgement

MS gratefully acknowledge Technische Universität Berlin for hosting this research and for providing the necessary computational infrastructure and institutional support. Parts of the manuscript were edited and refined with the assistance of an AI-based language model to improve clarity and readability; the scientific content, interpretations, and conclusions remain the sole responsibility of the author.

Financial support

This research was funded by the Alexander von Humboldt Foundation under a Humboldt Research Fellowship. HH acknowledges financial support from the Helmholtz Association's Initiative and Networking Fund for the Helmholtz Young Investigator Group ARES (contract number VH-NG-1516).

References

Alkhimenkov, Y., Khakimova, L., & Podladchikov, Y. (2021). Stability of discrete schemes of Biot's poroelastic equations. *Geophysical Journal International*, *225*(1), 354–377.

Bandis, S. C., Lumsden, A. C., & Barton, N. R. (1983). Fundamentals of rock joint deformation. *International Journal of Rock Mechanics and Mining Sciences & Geomechanics Abstracts*, *20*(6), 249–268. https://doi.org/10.1016/0148-9062(83)90595-8

Bommer, J. J. (2022). Earthquake hazard and risk analysis for natural and induced seismicity: Towards objective assessments in the face of uncertainty. *Bulletin of Earthquake Engineering*, *20*(6), 2825–3069.

Boyet, A., De Simone, S., Ge, S., & Vilarrasa, V. (2023). Poroelastic stress relaxation, slip stress transfer and friction weakening controlled post-injection seismicity at the Basel Enhanced Geothermal System. *Communications Earth & Environment*, *4*(1), 104. https://doi.org/10.1038/s43247-023-00764-y

Cao, W., Durucan, S., Shi, J.-Q., Cai, W., Korre, A., & Ratouis, T. (2022). Induced seismicity associated with geothermal fluids re-injection: Poroelastic stressing, thermoelastic stressing, or transient cooling-induced permeability enhancement? *Geothermics*, *102*, 102404.

Cheng, Y., Liu, W., Xu, T., Zhang, Y., Zhang, X., Xing, Y., Feng, B., & Xia, Y. (2023). Seismicity induced by geological CO2 storage: A review. *Earth-Science Reviews*, *239*, 104369.

Cueto-Felgueroso, L., Vila, C., Santillán, D., & Mosquera, J. C. (2018). Numerical Modeling of Injection-Induced Earthquakes Using Laboratory-Derived Friction Laws. *Water Resources Research*, *54*(12), 9833–9859. https://doi.org/10.1029/2017WR022363

Damirchi, B. V., Bitencourt, L. A. G., Manzoli, O. L., & Dias-da-Costa, D. (2022). Coupled hydro-mechanical modelling of saturated fractured porous media with unified embedded finite element discretisations. *Computer Methods in Applied Mechanics and Engineering*, *393*, 114804. https://doi.org/10.1016/j.cma.2022.114804

Dieterich, J. H. (1979). Modeling of rock friction: 1. Experimental results and constitutive equations. *Journal of Geophysical Research: Solid Earth*, *84*(B5), 2161–2168.

Dolbow, J., Moës, N., & Belytschko, T. (2000). Discontinuous enrichment in finite elements with a partition of unity method. *Finite Elements in Analysis and Design*, *36*(3–4), 235–260.

Erickson, B., Jiang, J., & Dunham, E. (2020). *SEAS Benchmark Problems BP3-QD and BP3-FD*.

Fries, T., & Belytschko, T. (2010). The extended/generalized finite element method: An overview of the method and its applications. *International Journal for Numerical Methods in Engineering*, *84*(3), 253–304.

Gerardi, G., Dublanchet, P., Jeannin, L., Kazantsev, A., Duboeuf, L., Ramadhan, I., Azis, H., Ganefianto, N., & Nugroho, I. A. (2024). Geomechanical modelling of injection-induced seismicity: The case study of the Muara Laboh geothermal plant. *Geophysical Journal International*, *237*(2), 818–837. https://doi.org/10.1093/gji/ggae084

https://doi.org/10.5194/egusphere-2026-1658
Preprint. Discussion started: 20 April 2026

Grigoli, F., Cesca, S., Priolo, E., Rinaldi, A. P., Clinton, J. F., Stabile, T. A., Dost, B., Fernandez, M. G., Wiemer, S., & Dahm, T. (2017). Current challenges in monitoring, discrimination, and management of induced seismicity related to underground industrial activities: A European perspective. *Reviews of Geophysics*, *55*(2), 310–340.

Grigoratos, I., Savvaidis, A., & Rathje, E. (2022). Distinguishing the causal factors of induced seismicity in the Delaware Basin: Hydraulic fracturing or wastewater disposal? *Seismological Research Letters*, *93*(5), 2640–2658.

Han, Z., & Younis, R. M. (2023). *Adaptive time-stepping to capture induced seismicity for unconventional reservoir exploration*. 361–371.

Hayek, J. N., May, D. A., Pranger, C., & Gabriel, A. (2023). A Diffuse Interface Method for Earthquake Rupture Dynamics Based on a Phase-Field Model. *Journal of Geophysical Research: Solid Earth*, *128*(12), e2023JB027143. https://doi.org/10.1029/2023JB027143

Heimisson, E. R., Liu, S., Lapusta, N., & Rudnicki, J. (2022). A Spectral Boundary-Integral Method for Faults and Fractures in a Poroelastic Solid: Simulations of a Rate-and-State Fault With Dilatancy, Compaction, and Fluid Injection. *Journal of Geophysical Research: Solid Earth*, *127*(9), e2022JB024185. https://doi.org/10.1029/2022JB024185

Hosseini, N., Paluszny, A., & Zimmerman, R. W. (2025). Dynamics of Fluid-Driven Slip on a 3D Heterogeneous Fault With Rate-and-State Friction. *Journal of Geophysical Research: Solid Earth*, *130*(7), e2025JB031221. https://doi.org/10.1029/2025JB031221

Im, K., & Avouac, J. (2025). Maximum Magnitude of Induced Earthquakes in Rate and State Friction Framework. *Seismological Research Letters*, *96*(3), 1654–1664.

Ito, S., Furui, K., & Tsusaka, K. (2023). Analysis of Fluid-Injection-Induced Seismicity Using Dynamic Sliding Model with Rate-And State-Dependent Friction Law. *SPE Annual Technical Conference and Exhibition*, D021S013R008. https://doi.org/10.2118/214891-MS

Ito, S., Furui, K., & Tsusaka, K. (2024). Analysis of Fluid-Injection-Induced Seismicity Using a Dynamic Sliding Model Incorporating the Rate-and State-Dependent Friction Law. *SPE J*, *29*(7), 3567–3583.

Jaeger, J. C., Cook, N. G., & Zimmerman, R. (2009). *Fundamentals of rock mechanics*. John Wiley & Sons.

Jin, L., & Zoback, M. D. (2018). Fully dynamic spontaneous rupture due to quasi-static pore pressure and poroelastic effects: An implicit nonlinear computational model of fluid-induced seismic events. *Journal of Geophysical Research: Solid Earth*, *123*(11), 9430–9468.

Khoei, A. R. (2015). *Extended finite element method: Theory and applications*. John Wiley & Sons, Inc. https://doi.org/10.1002/9781118869673

Kivi, I. R., Boyet, A., Wu, H., Walter, L., Hanson-Hedgecock, S., Parisio, F., & Vilarrasa, V. (2023). Global physics-based database of injection-induced seismicity. *Earth System Science Data*, *15*(7), 3163–3182.

Kontoe, S., Zdravkovic, L., Potts, D., & Menkiti, C. (2011). On the relative merits of simple and advanced constitutive models in dynamic analysis of tunnels. *Geotechnique*, *61*(10), 815–829.

Koutromanos, I. (2018). *Fundamentals of finite element analysis: Linear finite element analysis*. John Wiley & Sons.

Lapusta, N., & Liu, Y. (2009). Three-dimensional boundary integral modeling of spontaneous earthquake sequences and aseismic slip. *Journal of Geophysical Research: Solid Earth*, *114*(B9), 2008JB005934. https://doi.org/10.1029/2008JB005934

Liu, F., & Borja, R. I. (2009). An extended finite element framework for slow-rate frictional faulting with bulk plasticity and variable friction. *International Journal for Numerical and Analytical Methods in Geomechanics*, *33*(13), 1535–1560.

Liu, F., & Borja, R. I. (2010). Stabilized low-order finite elements for frictional contact with the extended finite element method. *Computer Methods in Applied Mechanics and Engineering*, *199*(37–40), 2456–2471. https://doi.org/10.1016/j.cma.2010.03.030

Liu, M., & Gorman, D. G. (1995). Formulation of Rayleigh damping and its extensions. *Computers & Structures*, *57*(2), 277–285.

Lysmer, J., & Kuhlemeyer, R. L. (1969). Finite dynamic model for infinite media. *Journal of the Engineering Mechanics Division*, *95*(4), 859–877.

https://doi.org/10.5194/egusphere-2026-1658
Preprint. Discussion started: 20 April 2026

Maddio, P. D., Sinatra, R., & Cammarata, A. (2025). A novel 2D penalty formulation for frictionless contact. *Multibody System Dynamics*, 1–25.

Moës, N., Dolbow, J., & Belytschko, T. (1999). A finite element method for crack growth without remeshing. *International Journal for Numerical Methods in Engineering*, *46*(1), 131–150.

Newmark, N. M. (1959). A method of computation for structural dynamics. *Journal of the Engineering Mechanics Division*, *85*(3), 67–94.

Riga, V. Yu., & Turuntaev, S. B. (2021). Induced Seismicity Modeling Based on Two-Parameter Rate-and-State Law. *Izvestiya, Physics of the Solid Earth*, *57*(5), 627–643. https://doi.org/10.1134/S1069351321050153

Romanet, P., Ampuero, J.-P., Cappa, F., Scuderi, M. M., & Chaillat, S. (2025). Combined boundary element and finite volume methods for modelling fluid-induced seismicity in fault networks within low-permeability rocks. *Geophysical Journal International*, *243*(3), ggaf377.

Ruina, A. (1983). Slip instability and state variable friction laws. *Journal of Geophysical Research: Solid Earth*, *88*(B12), 10359–10370.

Sabah. (2026). *MohammadSabah93/Hybrid-implicit-explicit-XFEM-simulation-of-injection-induced-seismicity: IMEX XFEM Initial Release* (Version V1.0.0) [Computer software]. Zenodo. https://doi.org/10.5281/ZENODO.19220256

Sabah, M., Hofmann, H., Cacace, M., Jalali, M. R., & Kivi, I. R. (2026). Modeling Injection-Induced Seismicity Using a Fully Coupled Poroviscoelasto-Dynamic Extended Finite Element Approach with Stabilized Contact and Rate-and-State Friction. *Computers and Geotechnics*, *191*, 107803.

Sun, W., Gu, Y. J., Liu, Y., Li, T., Wang, R., Wang, J., Harrington, R., Roth, M., Schultz, R., & Xu, G. (2026). Rupture cascade initiated by wastewater disposal: Nucleation and domino effect of Canada's largest induced earthquake. *Geophysical Research Letters*, *53*(1), e2025GL118405.

Templeton, D. C., Schoenball, M., Layland-Bachmann, C. E., Foxall, W., Guglielmi, Y., Kroll, K. A., Burghardt, J. A., Dilmore, R., & White, J. A. (2023). A project lifetime approach to the management of induced seismicity risk at geologic carbon storage sites. *Seismological Society of America*, *94*(1), 113–122.

Trutnevyte, E., & Ejderyan, O. (2018). Managing geoenergy-induced seismicity with society. *Journal of Risk Research*, *21*(10), 1287–1294.

Wang, H. (2000). *Theory of linear poroelasticity with applications to geomechanics and hydrogeology* (Vol. 2). Princeton university press.

Zhou, W., Lanza, F., Grigoratos, I., Schultz, R., Cousse, J., Trutnevyte, E., Muntendam-Bos, A., & Wiemer, S. (2024). Managing induced seismicity risks from enhanced geothermal systems: A good practice guideline. *Reviews of Geophysics*, *62*(4), e2024RG000849.

Zimmerman, R. W., & Paluszny, A. (2024). *Fluid flow in fractured rocks*. Wiley.